

Reciprocal interactions between innate immune cells and astrocytes facilitate neuroinflammation and brain metastasis via lipocalin-2

Received: 7 December 2021

Accepted: 17 January 2023

Published online: 16 February 2023

 Check for updates

Omer Adler^{1,14}, Yael Zait^{1,14}, Noam Cohen¹, Raquel Blazquez², Hila Doron¹, Lea Monteran¹, Yeela Scharff¹, Tamar Shami¹, Dhanashree Mundhe¹, Gunther Glehr³, Andrew A. Kanner⁴, Suzana Horn⁵, Vered Yahalom⁶, Sebastian Haferkamp⁷, James A. Hutchinson³, Annalen Bleckmann^{8,9,10}, Limor Nahary¹¹, Itai Benhar¹¹, Shlomit Yust Katz¹², Tobias Pukrop^{2,13} & Neta Erez¹✉

Brain metastasis still encompass very grim prognosis and therefore understanding the underlying mechanisms is an urgent need toward developing better therapeutic strategies. We uncover the intricate interactions between recruited innate immune cells and resident astrocytes in the brain metastatic niche that facilitate metastasis of melanoma and breast cancer. We show that granulocyte-derived lipocalin-2 (LCN2) induces inflammatory activation of astrocytes, leading to myeloid cell recruitment to the brain. LCN2 is central to inducing neuroinflammation as its genetic targeting or bone-marrow transplantation from LCN2^{-/-} mice was sufficient to attenuate neuroinflammation and inhibit brain metastasis. Moreover, high LCN2 levels in patient blood and brain metastases in multiple cancer types were strongly associated with disease progression and poor survival. Our findings uncover a previously unknown mechanism, establishing a central role for the reciprocal interactions between granulocytes and astrocytes in promoting brain metastasis and implicate LCN2 as a prognostic marker and potential therapeutic target.

Brain metastasis is one of the most lethal forms of cancer metastasis. Brain metastasis (BrM) is 2–10 times more frequent than primary central nervous system (CNS) tumors, with a grave median survival of less than 1 year^{1,2}. The incidence of BrM is increasing in recent years³, probably as a result of better diagnosis and improved control of extracranial disease by systemic therapy⁴. Therefore, better understanding of brain metastasis is an urgent unmet challenge.

The tumor microenvironment (TME) plays a crucial role in facilitating metastasis by promoting tumor cell invasion, survival and colonization at distant organs⁵. Moreover, studies of the pre-metastatic

niche suggested that modifications instigated by the primary tumor evoke early changes in the TME that predispose specific organs for metastases formation⁶. Both cancer and reactive stromal cells of the primary tumor secrete soluble factors that enable the formation of a hospitable metastatic niche at distant sites^{5,6}. Thus, understanding the early changes in the brain microenvironment that precede or facilitate BrM is of great clinical importance.

Recent studies have elucidated the important role of the brain microenvironment in facilitating brain metastatic relapse from various cancer types^{4,7–11}. Specifically, astrocytes, the most abundant glial cells

A full list of affiliations appears at the end of the paper. ✉ e-mail: netaerez@tauex.tau.ac.il

in the brain, were implicated as key components of the TME and shown to play a functional role in BrM^{4,12–18}. Their activation state is known as astrogliosis, characterized by neuroinflammation, which includes release of pro-inflammatory cytokines and chemokines, increased permeability of the blood–brain barrier and immune cell infiltration^{4,19}. Sustained neuroinflammation is present in acute and chronic brain pathologies, as well as in BrM^{4,15}; however, our knowledge on the events that initiate neuroinflammation in the brain metastatic niche and the early stages of BrM is still limited.

We previously established a model of spontaneous melanoma BrM in immune-competent mice and demonstrated early changes in the brain metastatic microenvironment, including activation of astrogliosis and pro-inflammatory signaling in astrocytes, associated with enhanced growth of melanoma cells in the brain²⁰. Using this platform, we showed that the CXCL10–CXCR3 signaling axis, physiologically important for recruitment of T cells, is hijacked by melanoma cells to facilitate brain tropism and metastasis¹³. We therefore hypothesized that either tumor or stromal cell-derived soluble factors instigate neuroinflammation in the brain metastatic niche and endeavored to characterize the underlying mechanism.

Here, we demonstrate that neuroinflammation that facilitates BrM from melanoma and breast cancer is driven by LCN2. LCN2, also known as neutrophil gelatinase-associated lipocalin (NGAL), is a secreted glycoprotein, initially identified in sequestering iron as a physiological response of the innate immune system in combating bacterial infections²¹. In the CNS, LCN2 was demonstrated to activate astrocytes and microglia^{22–24} and is implicated in multiple pathologies that involve neuroinflammation, including stroke, traumatic brain injury and neurodegenerative diseases²⁵; however, the role of LCN2 in BrM is largely unknown.

We show that systemic signaling derived from the primary tumor instigates pro-inflammatory activation of astrocytes. Activated astrocytes promoted the recruitment of immunosuppressive granulocytes to the brain metastatic microenvironment, which then become a main source of LCN2 signaling. Functionally, genetic targeting of LCN2 resulted in attenuated neuroinflammation and decreased BrM. Moreover, in blood and tissue samples from patients with BrM from multiple cancer types, systemic LCN2 levels were strongly correlated with disease progression and poor survival, positioning LCN2 as a potential prognostic marker for BrM.

Results

Systemic LCN2 is associated with brain metastasis

Seeking to uncover the mechanism by which neuroinflammation is activated in the brain metastatic niche, we utilized models of experimental BrM of melanoma and breast cancer (Fig. 1a). We analyzed the levels of

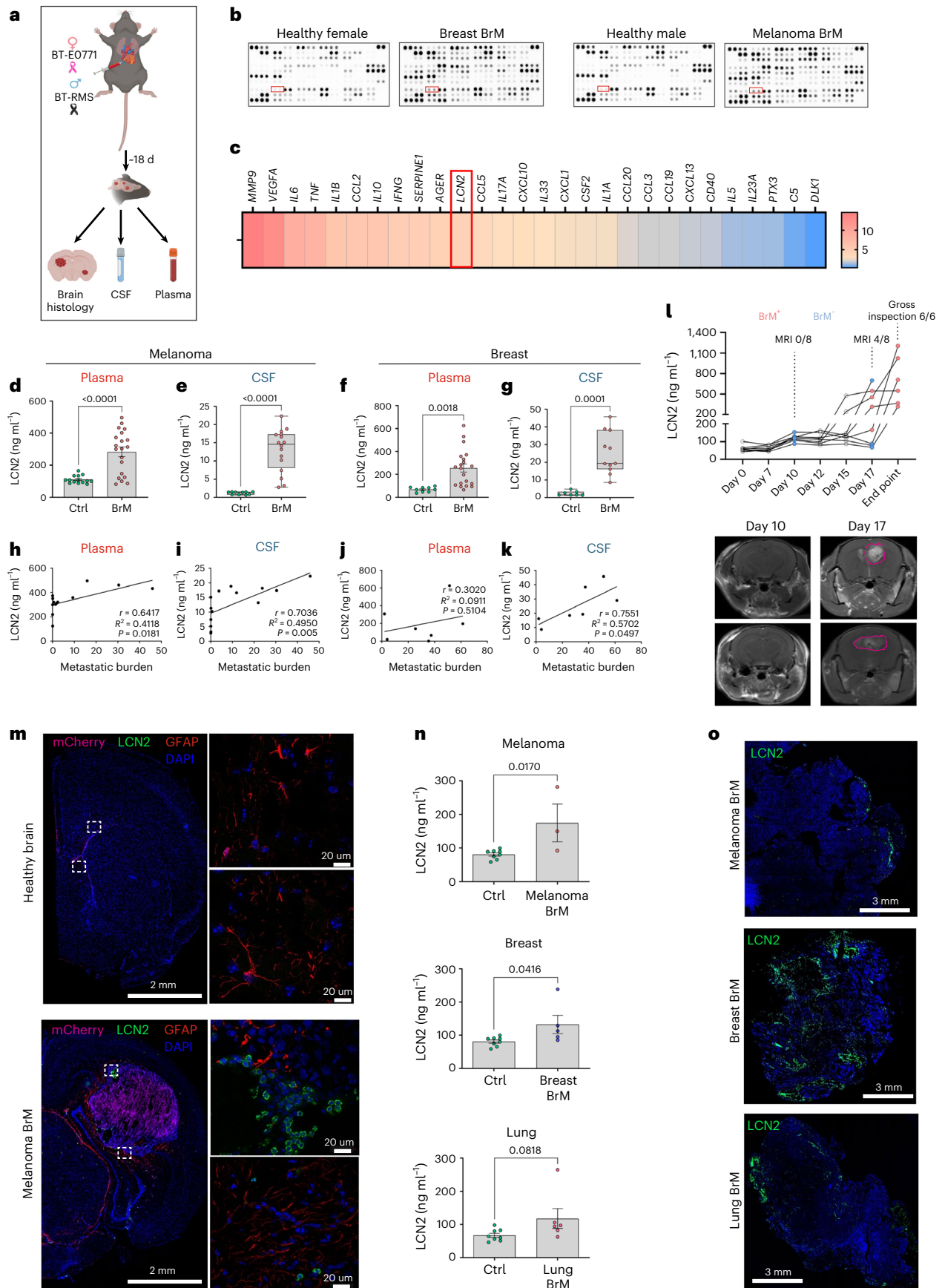
pro-inflammatory mediators in the blood of mice with melanoma or breast cancer BrM using the Proteome profiler Cytokine Array. Analysis of the results revealed multiple cytokines and chemokines that were upregulated in the blood of metastases-bearing mice (Extended Data Fig. 1 and Fig. 1b). Based on our previous studies showing that astrocyte activation precedes brain metastasis^{13,20}, we sought to identify potential mediators of astrocyte activation which could prepare the metastatic niche in the CNS. We therefore further analyzed the results using the VarElect tool²⁶, which enables prioritization of genes related to specific query terms. This analysis revealed known pro-inflammatory activators including matrix metalloproteinase (MMP)-9, interleukin (IL)-6, tumor necrosis factor (TNF), IL-1 β , interferon (IFN)- γ and LCN2 (Fig. 1c). We were intrigued by LCN2, as it was previously shown to be a mediator of astrocyte activation²⁷. Notably, MMP-9, which was the top protein on this list, has been shown to form a complex with LCN2 (ref. 28). The MMP-9–LCN2 complex promoted tumor growth and metastasis in several cancers, including breast, gastric and cholangiocarcinoma^{29–31}. Therefore, we focused our further investigations on LCN2 as a principal candidate for instigating neuroinflammation.

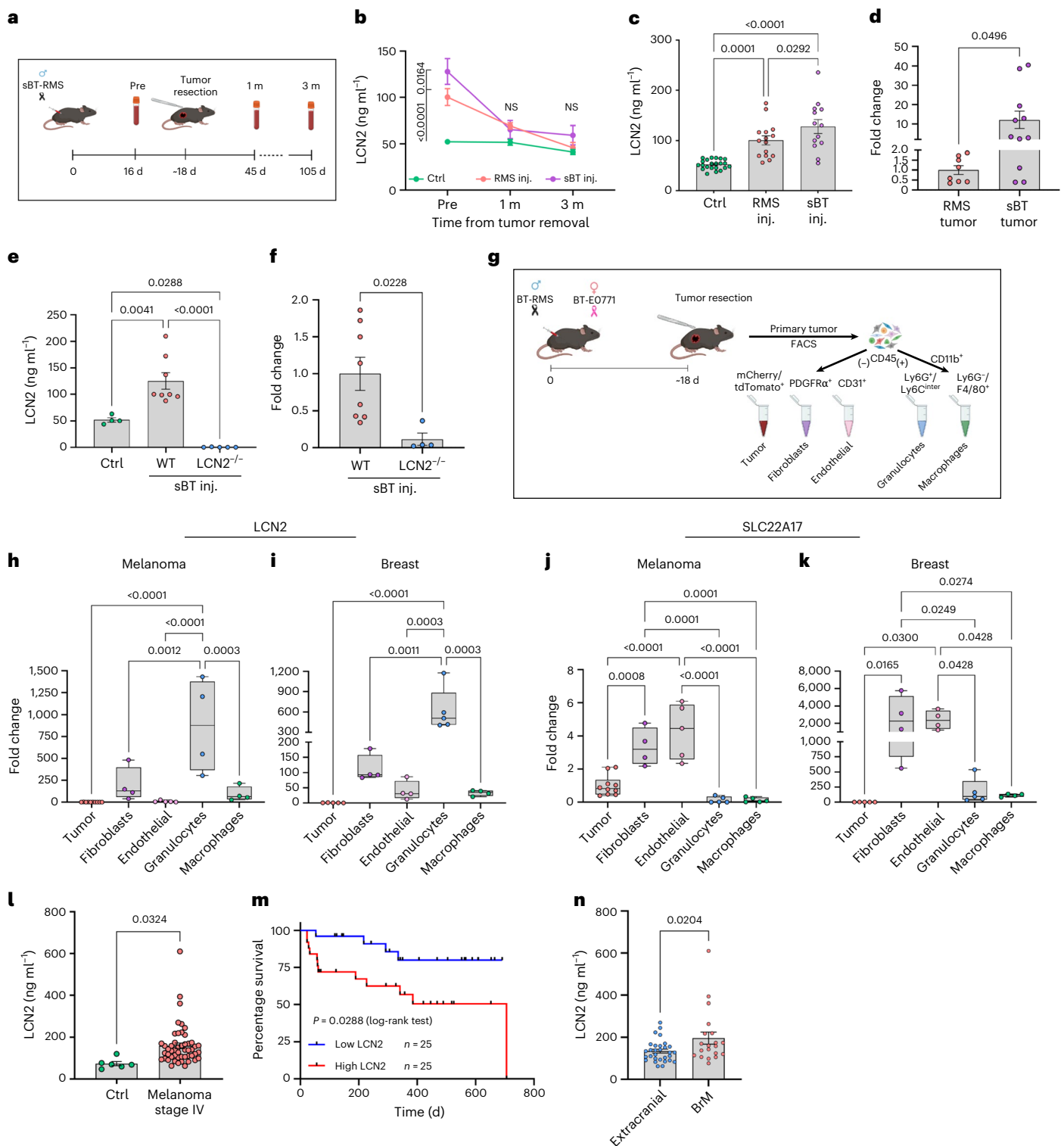
To assess systemic levels of LCN2, we analyzed LCN2 protein levels in plasma and in cerebrospinal fluid (CSF) of mice with BrM and found that LCN2 was systemically upregulated in blood and CSF of metastases-bearing mice in both melanoma (Fig. 1d,e) and breast cancer metastasis (Fig. 1f,g) compared to healthy mice. Notably, levels of LCN2 in blood and CSF in melanoma (Fig. 1h,i) and in breast cancer (Fig. 1j,k) correlated with brain metastatic burden, suggesting a link with disease progression. Moreover, to assess the temporal dynamic of LCN2 systemic upregulation, we injected mice with melanoma cells and performed longitudinal follow-up of their LCN2 blood levels and metastatic progression using magnetic resonance imaging (MRI). The results indicated that LCN2 levels were low until day 7 following injection and elevated gradually after day 10. Notably, elevation of LCN2 in the blood preceded the detection of brain metastasis by MRI (Fig. 1l). Furthermore, all the mice in which LCN2 levels were highly elevated developed BrM (excluding one mouse), further establishing systemic LCN2 as a predictive marker for BrM.

As LCN2 was prevalent in the CSF of metastases-bearing mice, we next asked whether LCN2 is expressed in the brain metastatic microenvironment. Immunostaining of LCN2 in metastases-bearing brains from melanoma confirmed that LCN2 was highly abundant in the brain metastatic microenvironment, but not in healthy brains (Fig. 1m). We validated these findings in humans by analyzing LCN2 levels in blood samples from patients with brain metastasis from melanoma, breast cancer or lung carcinoma (Extended Data Table 1). The results confirmed that LCN2 is systemically upregulated in patients with BrM compared to healthy controls (Fig. 1n). Moreover, immunostaining

Fig. 1 | Systemic LCN2 signaling is upregulated in plasma and CSF in brain metastases and correlates with metastatic burden. **a**, Experimental scheme. Mice were analyzed 18 d after intracardiac injection with BT-RMS or BT-EO771 cells. **b**, Expression of 111 soluble proteins in the blood of mice with breast cancer (left) or melanoma (right) brain metastases was analyzed using the Proteome profiler Cytokine Array. Sex-matched healthy mice were used as control (healthy, $n = 6$ mice; breast BrM, $n = 9$ mice; melanoma BrM, $n = 10$ mice). **c**, VarElect analysis of neuroinflammation-related genes that were upregulated at least twofold in the Cytokine Array. Heat map shows ranking of connection between the genes and the query terms used for analysis. **d**, LCN2 plasma levels measured by ELISA in mice with melanoma BrM. Dots represent individual mice, error bars represent s.e.m. ($n = 14$, 20 mice; one-way analysis of variance (ANOVA)). **e**, LCN2 CSF levels measured by ELISA in mice with melanoma BrM. Dots represent individual mice, line indicates median, whisker shows mean to max ($n = 10$, 16 mice; one-way ANOVA). **f**, LCN2 plasma levels measured by ELISA in mice with breast cancer BrM. Dots represent individual mice, error bars represent s.e.m. ($n = 9$, 20 mice; one-way ANOVA). **g**, LCN2 CSF levels measured by ELISA in mice with breast cancer BrM. Dots represent individual mice, line indicates median, whisker shows mean to max ($n = 7$, 11 mice; one-way ANOVA).

h,i, Two-sided Pearson correlation between LCN2 plasma (**h**) or CSF (**i**) levels and brain metastatic burden ($n = 13$ mice). **j,k**, Two-sided Pearson correlation between LCN2 plasma (**j**) or CSF (**k**) levels and brain metastatic burden ($n = 7$ mice). **l**, Longitudinal LCN2 plasma levels measured by ELISA in mice injected intracardially with BT-RMS cells. Plasma was collected on different time points. BrM was detected by MRI as indicated and verified by gross inspection at end point ($n = 8$ mice). **m**, Immunofluorescence of LCN2, GFAP (astrocytes) and mCherry (cancer cells) in brains from healthy mice or mice with BrM. White boxes indicate areas magnified (right). Representative images from $n = 3$ sections in $n = 2$ mice were analyzed. Scale bar, 2 mm; magnification, 20 μ m. DAPI, 4,6-diamidino-2-phenylindole. **n**, ELISA assay for human LCN2 plasma levels of patients with BrM from melanoma ($n = 3$ patients), breast ($n = 5$ patients) and lung ($n = 6$ patients) compared to healthy controls (Ctrl) ($n = 8$ patients). Dots represents individual patients, error bars represent s.e.m. (Student's *t*-test, two-sided). **o**, Immunofluorescence of LCN2 in frozen sections of resected human brain metastases from patients with melanoma, breast and lung cancer, representative images are shown from $n = 2$ patients samples stained per cancer type. Scale bar, 3 mm. Graphical illustrations were created with BioRender.com.





of brain tissue sections from these patients indicated that LCN2 is expressed in human BrM (Fig. 10). Taken together, these findings suggest a functional role for LCN2 in facilitating brain metastasis.

LCN2 is secreted by stromal cells in the primary tumor

As we previously observed that inflammatory signaling in the brain precedes the formation of macrometastases, we next asked whether LCN2 in the blood is secreted from the primary tumor. We analyzed the levels of LCN2 in the blood of mice injected orthotopically with Ret-melanoma-sorted (RMS) melanoma cells, followed by resection of the primary tumor (Fig. 2a). Notably, we found that blood levels of

LCN2 were elevated in tumor-bearing mice, but decreased to basal levels following primary tumor resection (Fig. 2b). Moreover, the expression and secretion of LCN2 in primary tumors derived from brain-tropic cells (sBT-RMS cells, isolated from spontaneous BrM¹³), were significantly elevated compared to that of parental cells (Fig. 2c,d). Intrigued by these findings, we next asked whether LCN2 is derived from cancer or host cells in the primary tumor. To test this, we orthotopically inoculated wild-type (WT) or *Lcn2*^{-/-} mice with melanoma sBT-RMS cells and analyzed the expression and secretion of LCN2 in primary tumors. Analysis of the results revealed that tumors resected from *Lcn2*^{-/-} mice had almost no LCN2 (Fig. 2e,f), implying that host cells in the TME are

Fig. 2 | LCN2 is systemically secreted by the microenvironment of primary tumors, upregulated in brain-tropic tumors and correlates with patient survival. **a**, Experimental scheme analyzed in **b–d**. **b**, LCN2 plasma levels measured by ELISA in mice injected with RMS or sBT-RMS cells at different time points. Error bars represent s.e.m. (Ctrl $n = 22, 15, 7$ mice; RMS $n = 15, 21, 7$ mice; sBT $n = 13, 10, 10$ mice; repeated measure ANOVA). NS, not significant; inj., injected. **c**, LCN2 plasma levels measured by ELISA before primary tumor resection. Dots represent individual mice, error bars represent s.e.m. (Ctrl $n = 22$ mice; RMS $n = 15$ mice; sBT $n = 13$ mice; one-way ANOVA). **d**, *Lcn2* expression in primary tumors from RMS- or sBT-RMS-injected mice. Dots represent individual mice, error bars represent s.e.m. (RMS $n = 8$ mice; sBT $n = 11$ mice; Student's *t*-test, two-sided). **e**, LCN2 plasma levels measured by ELISA from WT or *Lcn2*^{-/-} mice with primary tumor (p.tumor). Dots represent individual mice, error bars represent s.e.m. (WT healthy $n = 4$ mice; WT p.tumor $n = 8$ mice; *Lcn2*^{-/-} p.tumor $n = 5$ mice; one-way ANOVA). **f**, *Lcn2* expression in primary tumors from WT or *Lcn2*^{-/-} mice. Dots represent individual mice, error bars represent s.e.m. (WT $n = 8$ mice; *Lcn2*^{-/-} $n = 4$ mice; Student's *t*-test, two-sided). **g**, Experimental scheme analyzed in **h–k**. **h, i**, *Lcn2* expression in different cell populations

from **g**; dots represent individual mice, line indicates median, whisker shows mean to max (tumor $n = 10/5$ mice; fibroblasts $n = 4$ mice; endothelial $n = 5/4$ mice; granulocytes $n = 4/5$ mice; macrophages $n = 4$ mice; one-way ANOVA). **j, k**, *Slc22a17* expression in different cell populations from **g**, dots represent individual mice, line indicates median, whisker shows mean to max (tumor $n = 10/5$ mice; fibroblasts $n = 4$ mice; endothelial $n = 5/4$ mice; granulocytes $n = 4/5$ mice; macrophages $n = 4$ mice; one-way ANOVA). **l**, LCN2 plasma levels measured by ELISA from patients diagnosed with stage IV melanoma before treatment ($n = 50$ patients), or healthy controls ($n = 6$ patients). Dots represent individual patients; error bars represent s.e.m. (Student's *t*-test). **m**, Survival curve analysis of patients with low versus high LCN2 blood levels in stage IV melanoma analyzed in **l**. The cutoff was determined by the median LCN2 level ($n = 25$ patients per group; Kaplan–Meier curve, log-rank test). **n**, LCN2 plasma levels measured by ELISA from patients in stage IV melanoma analyzed in **l**. Patients were divided according to their BrM status: extracranial ($n = 30$ patients) or intracranial ($n = 20$ patients). Dots represent individual patients; error bars represent s.e.m. (Student's *t*-test). Graphical illustrations were created with BioRender.com.

the main source of systemic LCN2 signaling. To further characterize the cellular source of LCN2 in the primary TME, we injected mice orthotopically with melanoma or breast cancer cells and isolated distinct cell populations from resected tumors including CD45⁻mCherry/tdTomato⁺ tumor cells, CD45⁺PDGFR α ⁺ fibroblasts, CD45⁻CD31⁺ endothelial cells, CD45⁺Ly6G⁺Ly6C^{int} granulocytes and CD45⁺Ly6G⁺F480⁺ macrophages (Fig. 2g and Extended Data Fig. 2a). We found that in both melanoma and breast tumors, the main cellular origins of *Lcn2* were fibroblasts and granulocytes (Fig. 2h, i). Notably, the expression of *Lcn2* was induced in primary dermal fibroblasts, bone-marrow-derived monocytes and endothelial cells by tumor cell-secreted factors in vitro (Extended Data Fig. 2b–d), suggesting that stromal LCN2 signaling is activated by the cancer cells. Moreover, brain-tropic cancer cells could instigate higher levels of *Lcn2* in fibroblasts (Extended Data Fig. 2e), in agreement with our observation that sBT-RMS tumors contained higher levels of LCN2 (Fig. 2c, d). To get further insight on LCN2 signaling we analyzed the expression of *Slc22a17*, the receptor of LCN2 (refs. ^{32,33}) and found that it was mainly expressed on endothelial cells and fibroblasts in both melanoma and breast cancer (Fig. 2j, k). We next asked whether LCN2 signaling is functionally important for primary tumor growth. Of note, analysis of primary tumor growth revealed no significant differences between tumors in WT and *Lcn2*^{-/-} mice in both melanoma (Extended Data Fig. 2f) and mammary tumors (Extended Data Fig. 2g). We further assessed whether systemic LCN2 is also evident in human patients with melanoma at time of diagnosis and whether its secretion from human primary melanoma tumors could be a prognostic factor. We obtained blood samples from a cohort of patients diagnosed with stage IV melanoma, before treatment and analyzed their LCN2 levels (Extended

Data Table 2). The findings indicated that patients with melanoma had significantly higher blood levels of LCN2 compared to healthy controls (Fig. 2l). Moreover, high blood levels of LCN2 correlated with worse survival (Fig. 2m). To test whether LCN2 blood levels are indicative of brain metastatic relapse, we stratified the patients with melanoma according to their long-term metastatic progression, namely patients who eventually developed BrM versus patients with extracranial metastatic disease. Notably, patients who developed BrM presented with significantly higher levels of LCN2 before diagnosis of BrM (Fig. 2n).

Thus, LCN2 is systemically secreted from stromal cells in primary tumors, giving rise to high blood levels in tumor-bearing mice or patients with melanoma, suggesting that LCN2 could serve as a prognostic marker at the time of diagnosis and as a predictive marker of brain metastatic relapse.

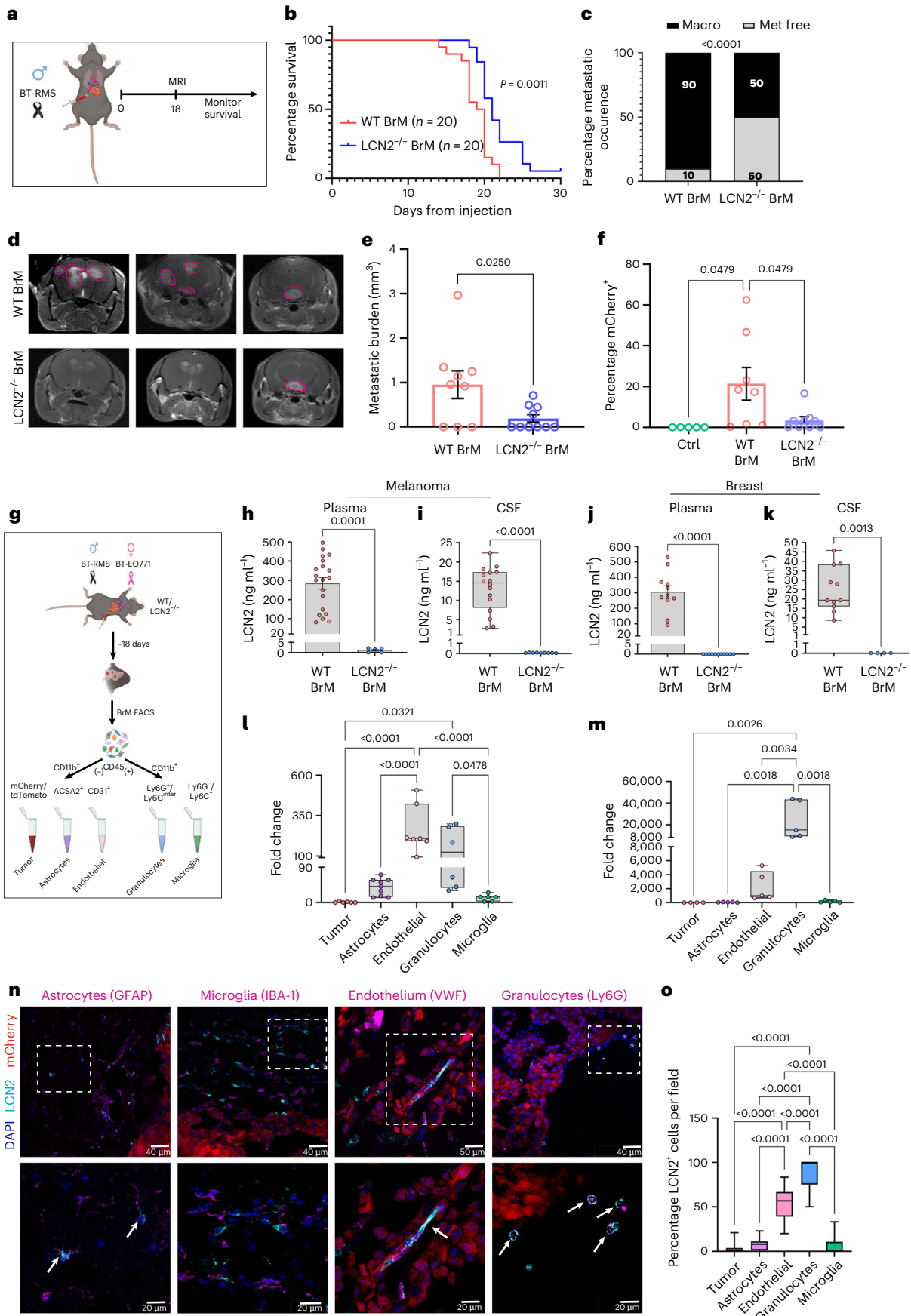
LCN2 is functionally important for brain metastasis

On the basis of high levels of LCN2 in mice with BrM, we hypothesized that LCN2 may be functionally important for brain metastatic growth. To test this, we analyzed metastases-bearing brains from melanoma and breast cancer in WT or *Lcn2*^{-/-} mice. Notably, we found that the survival of WT mice with melanoma BrM was reduced compared to *Lcn2*^{-/-} mice, consistent with a dramatic decrease in the percentage of mice with macrometastases in *Lcn2*^{-/-} mice (Fig. 3a–c). Moreover, analysis of metastatic burden by MRI confirmed that WT mice had more metastatic lesions (Fig. 3d, e). This was further supported by quantification of mCherry⁺ tumor cells in brains of WT or *Lcn2*^{-/-} mice (Fig. 3f), implicating LCN2 as an important mediator of BrM formation. Analysis of metastases-bearing brains in WT or *Lcn2*^{-/-} mice with breast

Fig. 3 | LCN2 signaling is functionally important for brain metastases formation and originates mainly from granulocytes and endothelial cells.

a, Experimental scheme analyzed in **b–f**. **b**, Survival curve analysis of WT and *Lcn2*^{-/-} mice injected intracardially with BT-RMS cells. Two independent experiments (WT $n = 20$ mice; *Lcn2*^{-/-} $n = 19$ mice; Kaplan–Meier curve, log-rank test). **c**, Brain macrometastases incidence defined by positive MRI and/or gross inspection (WT $n = 20$ mice; *Lcn2*^{-/-} $n = 20$ mice; analysis of contingency, chi-squared, one-sided). **d, e**, Representative MRI and quantification of metastatic area in WT and *Lcn2*^{-/-} mice ($n = 9/10$ mice, respectively). Dots represent individual mice, error bars represent s.e.m. (Student's *t*-test, two-sided). **f**, Brain metastatic burden quantified by FACS in mice analyzed in **d**. Dots represent individual mice, error bars represent s.e.m. ($n = 5$ mice, $n = 9$ mice, $n = 10$ mice, respectively; one-way ANOVA). **g**, Experimental scheme analyzed in **h–m**. **h, j**, LCN2 plasma levels of mice from **g** measured by ELISA. Dots represent individual mice, error bars represent s.e.m. (melanoma $n = 20, 5$ mice), (breast $n = 11, 11$ mice) (Student's *t*-test, two-sided). **i, k**, LCN2 CSF levels of mice from **g** measured by ELISA. Dots represent individual mice, line indicates median, whisker shows

mean to max (melanoma $n = 16, 9$ mice), (breast $n = 11, 4$ mice) (Student's *t*-test, two-sided). **l, m**, *Lcn2* expression in FACS-sorted cell populations from brains of mice described in **g**; dots represent individual mice, line indicates median, whisker shows mean to max (tumor $n = 6/4$ mice; astrocytes $n = 9/5$ mice; endothelial $n = 7/5$ mice; granulocytes $n = 6/5$ mice; microglia $n = 6/5$ mice; one-way ANOVA). **n**, Immunofluorescence in frozen sections of mice with melanoma BrM. Colocalization of LCN2 with specific cell markers: GFAP (astrocytes), IBA-1 (microglia), mCherry (melanoma), VWF (endothelial cells) and Ly6G (granulocytes). Representative images are shown from multiple sections analyzed in $n = 3$ mice. Dashed rectangles mark areas enlarged in lower panel. Scale bar 40/50 μ m (top), 20 μ m (bottom). **o**, Quantification of **n**. Colocalization of LCN2 with specific cell types, quantified as ratio between number of double-positive cells and the total number of specific cell type per field. Representative images are shown from $n = 4$ mice. Seven fields \times one section per mouse were analyzed, line indicates median, whisker shows mean to max (one-way ANOVA). Graphical illustrations were created with BioRender.com.



cancer BrM indicated no significant differences in survival and brain metastatic burden (Extended Data Fig. 3a–c), suggesting that additional pathways may be operative in breast cancer metastasis.

To get mechanistic insight on the role of LCN2 signaling in brain metastasis, we next isolated blood, CSF and multiple cell populations from the brain microenvironment in metastases-bearing WT or *Lcn2*^{-/-} mice: CD45⁺mCherry/tdTomato⁺ cancer cells, CD45⁺ACSA2⁺ astrocytes, CD45⁺CD31⁺ endothelial cells, CD45⁺Ly6G⁺Ly6C^{int} granulocytes and CD45⁺Ly6G⁻Ly6C⁻ microglia/monocyte-derived macrophages (MG/MDM) (Fig. 3g and Extended Data Fig. 3d). In agreement with our findings from primary tumor, the results confirmed that LCN2 is almost exclusively host-derived in both melanoma and breast cancer BrM (Fig. 3h–k). Moreover, detailed analysis of *Lcn2* expression in specific cell types from melanoma or breast cancer BrM indicated that granulocytes and endothelial cells are the main source of LCN2 (Fig. 3l,m). This was further validated by immunostaining of melanoma BrM, which confirmed that *Lcn2* is most abundantly expressed in granulocytes and endothelial cells (Fig. 3n,o). Thus, LCN2 in BrM is secreted mostly by recruited granulocytes and brain endothelial cells and is functionally important for BrM formation.

Granulocytes instigate inflammatory activation of astrocytes

To decipher the mechanism by which LCN2 facilitates brain metastatic growth, we next asked which cells in the brain respond to LCN2 signaling. We isolated cells from the brain metastatic microenvironment as above and analyzed the expression of *Slc22a17*, the specific LCN2 receptor. In both melanoma and breast cancer metastases, the highest expression of the LCN2 receptor was in astrocytes and to a lesser extent in endothelial cells and microglia (Fig. 4a,b). Moreover, we analyzed the expression of the LCN2 receptor in a dataset of human patients with BrM from melanoma, lung and breast cancer, as well as in primary brain tumors¹⁰ and found that its expression was highest in CD45⁻ stromal cells (Fig. 4c and Extended Data Fig. 4a). Based on these findings we hypothesized that granulocyte-derived LCN2 instigates pro-inflammatory signaling in astrocytes, leading to activation of neuroinflammation in the brain metastatic niche. To test this, we produced recombinant LCN2. Incubation of primary astrocytes isolated from adult mouse brains with rLCN2 confirmed that LCN2 was sufficient to upregulate the expression of multiple inflammatory cytokines and chemokines in astrocytes (Extended Data Fig. 4b). To test whether LCN2-induced activation of astrocytes is mediated by the SLC22A17 receptor, we specifically knocked down (KD) the expression of *Slc22a17* in primary adult astrocytes using short-interfering (si)RNA transduction and assessed the effect of this KD on LCN2-mediated pro-inflammatory activation. Analysis of the expression of multiple cytokines and chemokines, calculated as a combined ‘inflammatory score’ revealed that KD of the LCN2 receptor on astrocytes inhibited the upregulation of the ‘inflammatory score’ by LCN2 (Fig. 4d and Extended Data Fig. 4c). These findings confirm the importance of the LCN2–SLC22A17 axis in astrocyte activation during BrM.

Because we found that the main source of LCN2 in the brain is from recruited granulocytes, we further characterized the intricate

interactions between granulocytes and astrocytes. We established in vitro assays where primary astrocytes were incubated with secreted factors from bone-marrow-derived granulocytes that were activated with melanoma cell-conditioned medium (CM) (Fig. 4e). ELISA assays for LCN2 confirmed that primary granulocytes are activated by tumor cellCM to secrete LCN2 (Extended Data Fig. 4d). We found that secreted factors from tumor-activated granulocytes instigated inflammatory signaling in astrocytes, evident by upregulation of multiple cytokines and chemokines (Fig. 4f). To further investigate whether granulocyte-mediated activation of astrocytes is LCN2-dependent, we assessed in vivo the activation and inflammatory status of metastases-associated astrocytes. We initially analyzed the expression of glial fibrillary acidic protein (GFAP), a hallmark marker of astrocyte activation³⁴, in WT versus *Lcn2*^{-/-} mice with BrM. Analysis of GFAP staining in brain tissue sections indicated that astrocytes in WT mice with BrM were significantly more activated compared to *Lcn2*^{-/-} mice (Extended Data Fig. 4e,f). To assess the importance of LCN2 for pro-inflammatory activation of astrocytes, we isolated astrocytes from BrM of WT or *Lcn2*^{-/-} mice. The results indicated that pro-inflammatory signaling was significantly lower in astrocytes isolated from *Lcn2*^{-/-} mice in both melanoma and breast cancer metastasis (Fig. 4g,h and Extended Data Fig. 4g,h). Moreover, analysis of the combined ‘inflammatory score’ confirmed that inflammatory signaling was lower in astrocytes isolated from *Lcn2*^{-/-} mice, in both melanoma and breast cancer metastasis (Fig. 4i,j), suggesting that LCN2 plays an important role in inflammatory activation of metastases-associated astrocytes. Of note, these changes in astrocytes were metastasis-specific, as lack of LCN2 did not affect the activation status of healthy astrocytes (Extended Data Fig. 4i). Furthermore, LCN2-mediated signaling in brain were receptor-specific, as microglia cells, which express low levels of the LCN2 receptor did not exhibit differential activation in WT versus *Lcn2*^{-/-} mice (Extended Data Fig. 4j,k). Thus, although recruited granulocytes secrete a plethora of chemokines and cytokines, lack of LCN2 was sufficient to inhibit pro-inflammatory activation of astrocytes in BrM, implicating granulocyte-derived LCN2 as central mediator of inflammatory activation in astrocytes.

Taken together, these results demonstrate that LCN2, secreted by recruited myeloid cells in the brain metastatic microenvironment instigates pro-inflammatory signaling in astrocytes via the LCN2 receptor.

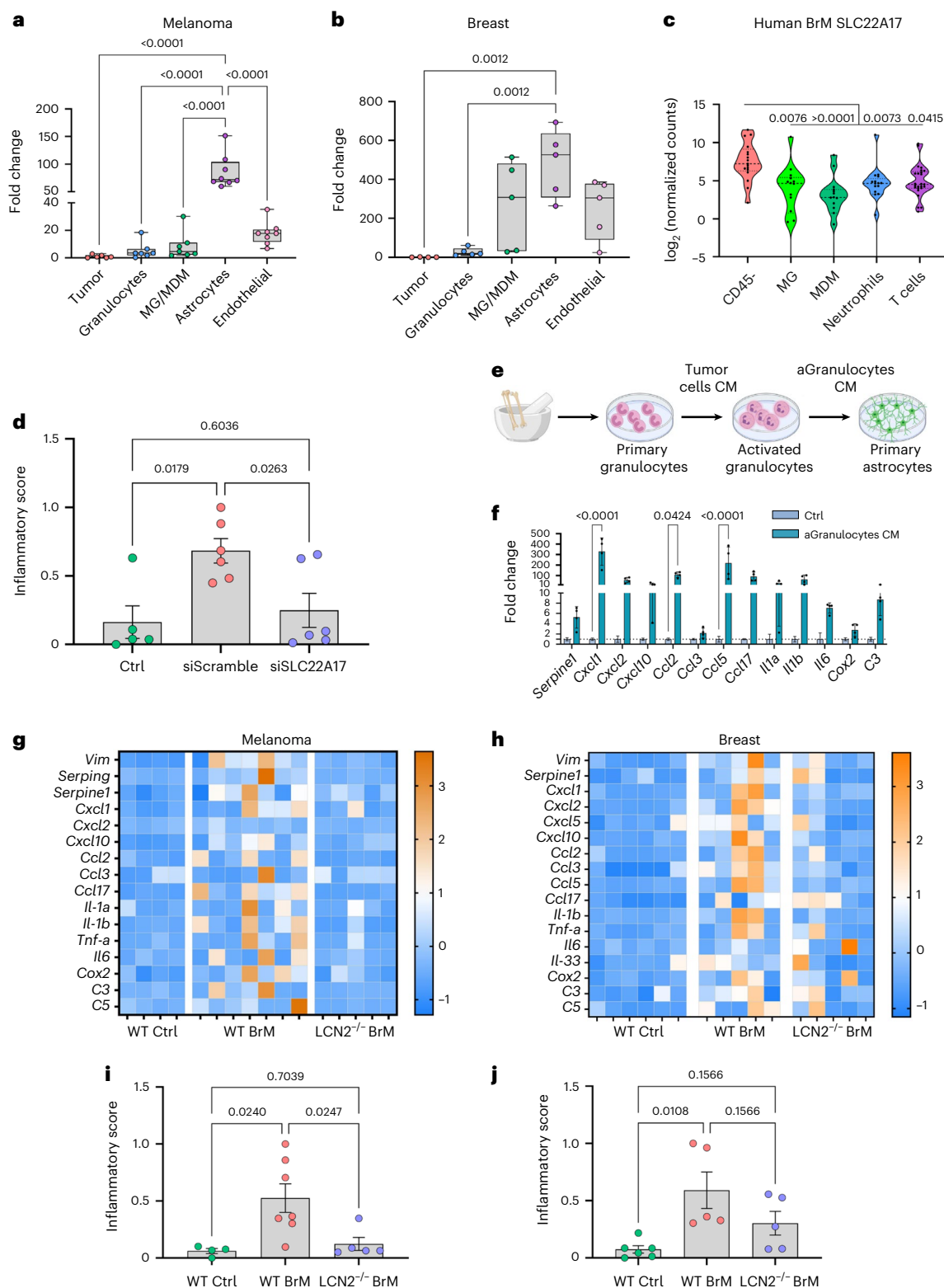
As many of the pro-inflammatory genes activated in metastases-associated astrocytes are known chemoattractants for innate immune cells, we hypothesized that inflammatory activation of astrocytes facilitates BrM via the recruitment of tumor-promoting immune cells. To test this, we initially tested the ability of LCN2 to induce myeloid cell recruitment by astrocytes. Astrocytes were incubated with rLCN2 or left untreated and their effect on recruitment of bone-marrow-derived monocytes or granulocytes was quantified. The results confirmed that LCN2 was sufficient to induce granulocyte migration toward astrocytes (Extended Data Fig. 5a). Therefore, we next asked whether LCN2 is functionally important for myeloid cell recruitment. We examined the immune milieu in brains of WT or *Lcn2*^{-/-} mice with BrM. Analysis of myeloid cells in melanoma BrM revealed that

Fig. 4 | Inflammatory activation of astrocytes is partially mediated by specific LCN2 receptor signaling. **a,b**, *Slc22a17* expression in FACS-sorted cell populations from whole brains of mice with BrM following BT-RMS or BT-EO771 injection. Dots represents individual mice, line indicates median, whisker shows mean to max (tumor $n = 6/4$ mice; astrocytes $n = 8/5$ mice; endothelial $n = 8/5$ mice; granulocytes $n = 7/5$ mice; microglia $n = 7/5$ mice; one-way ANOVA). **c**, *Slc22a17* expression in bulk RNA-seq of different cell populations isolated from samples of human BrM (brain TIME dataset). Dots represents individual patients (CD45⁻ $n = 17$ patients; MG $n = 14$ patients; MDM $n = 13$ patients; neutrophils $n = 17$ patients; T cells $n = 25$ patients; one-way ANOVA). **d**, qPCR analysis of inflammatory gene signature, calculated as ‘inflammatory score’ in primary astrocytes transfected with siRNA targeting *Slc22a17* or with control siRNA (si*Slc22a17* or siScramble). Error bars represent mean \pm s.d.; three biological

repeats in duplicate (one-way ANOVA). **e**, Experimental scheme analyzed in **f**. **f**, qPCR analysis of inflammatory gene signature in primary astrocytes incubated with CM from activated granulocytes. Error bars represent s.d. Dots represents different biological repeats (Ctrl $n = 3$ biological replicates; granulocyte CM $n = 4$ biological replicates; two-way ANOVA). **g,h**, qPCR analysis of inflammatory gene signature in FACS-sorted astrocytes from WT or *Lcn2*^{-/-} mice with BrM, following BT-RMS or BT-EO771 injection. Heat maps represent z score of individual genes (melanoma: Ctrl $n = 4$ mice; WT $n = 7, 10$ mice; *Lcn2*^{-/-} $n = 5, 9$ mice; and breast: Ctrl $n = 6$ mice; WT $n = 5$ mice; *Lcn2*^{-/-} $n = 5, 7$ mice). **i,j**, qPCR analysis of inflammatory gene signature of mice in **g,h**, calculated as ‘inflammatory score’. Error bars represent s.e.m. (one-way ANOVA). Graphical illustrations were created with BioRender.com.

while both granulocytes (Ly6G⁺Ly6C^{int}) and monocytes (Ly6C⁺Ly6G⁻) were elevated in BrM, their recruitment was inhibited in brains of *Lcn2*^{-/-} mice (Fig. 5a–d), implying that LCN2 is functionally important for their recruitment to the brain metastatic niche. Notably, pro-inflammatory activation of astrocytes plays an important role in recruitment of granulocytes to the brain metastatic microenvironment, as the inflammatory score of astrocytes significantly correlated with neutrophil infiltration (Fig. 5e). Furthermore, the percentages of granulocytes

and monocytes correlated with metastatic burden in melanoma BrM (Fig. 5f,g), suggesting a functional role for recruited myeloid cells in facilitating metastatic growth. Of note, analysis of bone marrow in WT versus *Lcn2*^{-/-} mice revealed no differences in immune cell composition, confirming that the differences in BrM resulted from differential recruitment of bone-marrow-derived cells in WT or *Lcn2*^{-/-} mice, rather than differences in their bone-marrow prevalence (Extended Data Fig. 5b). Moreover, analysis of healthy brains from WT or *Lcn2*^{-/-} mice



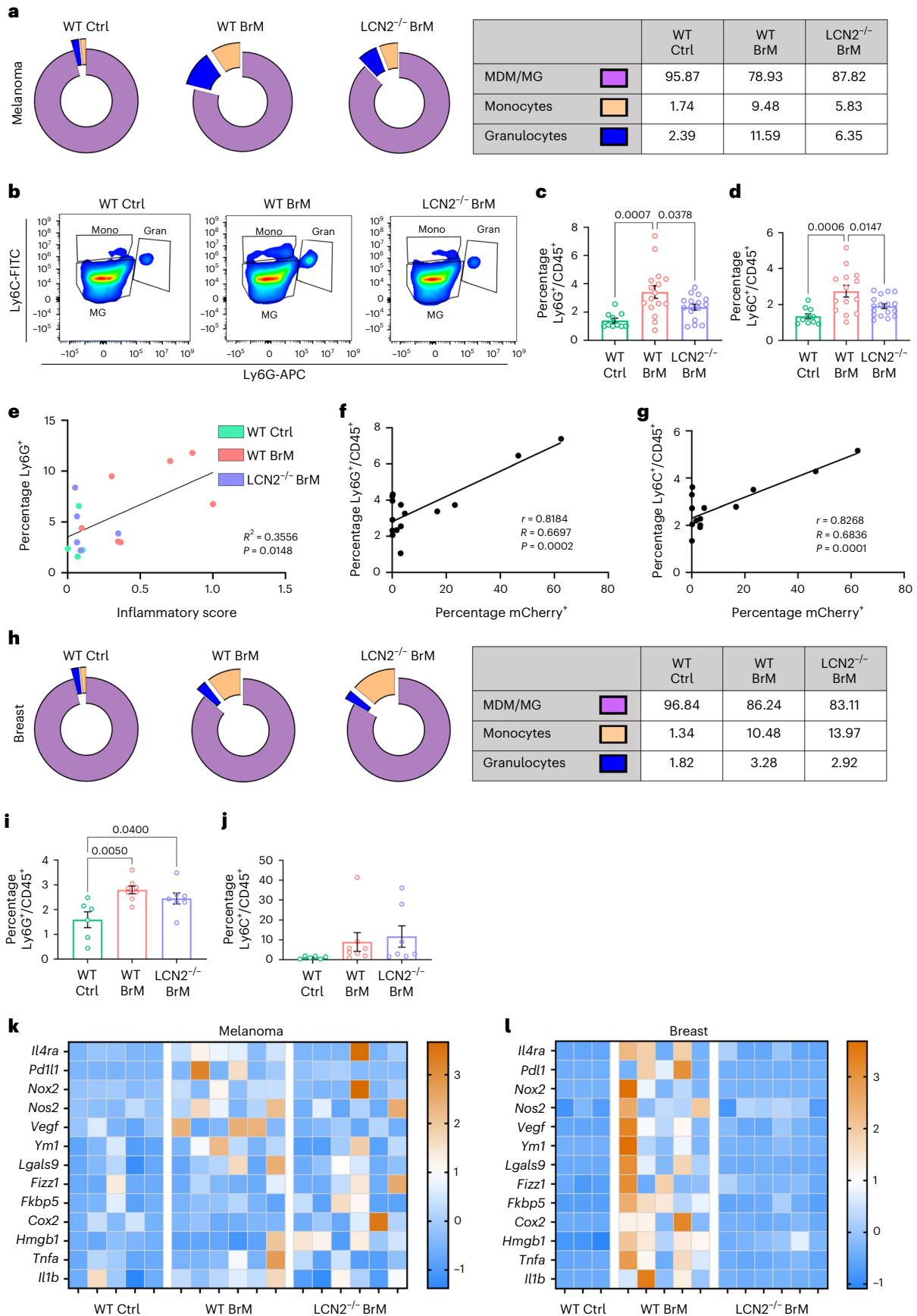


Fig. 5 | LCN2 signaling facilitates recruitment of immune suppressive myeloid cells into brain metastases. **a, b**, Immune profiling of CD11b⁺ myeloid cells by flow cytometry of BrM in WT or *Lcn2*^{-/-} mice injected with BT-RMS cells (Ctrl *n* = 5 mice; WT *n* = 9 mice; *Lcn2*^{-/-} *n* = 9 mice). **c, d**, Flow cytometry analysis of CD45⁺CD11b⁺Ly6C^{inter}Ly6G⁺ granulocytes and CD45⁺CD11b⁺Ly6C⁺Ly6G⁻ monocytes in brains from WT or *Lcn2*^{-/-} mice. Dots represent individual mice and error bars represent s.e.m. (Ctrl *n* = 10 mice; WT *n* = 16, 14 mice; *Lcn2*^{-/-} *n* = 16, 17 mice; one-way ANOVA). **e**, Two-sided Pearson correlation between the 'inflammatory score' in sorted astrocytes and percentage of granulocytes in brains of mice from Fig. 4g–j (Ctrl *n* = 4 mice; WT *n* = 7 mice; *Lcn2*^{-/-} *n* = 5 mice). **f, g**, Two-sided Pearson correlation between percentage of granulocytes and monocytes and brain metastatic load, quantified by percentage mCherry⁺ cells in brains of mice

from **a, b** (*n* = 15 mice per group). **h**, Immune profiling of CD11b⁺ myeloid cells by flow cytometry of BrM in WT or *Lcn2*^{-/-} mice injected with BT-E0771 cells (Ctrl *n* = 6 mice; WT *n* = 8 mice; *Lcn2*^{-/-} *n* = 7 mice). **i, j**, Flow cytometry analysis of CD45⁺CD11b⁺Ly6C^{inter}Ly6G⁺ granulocytes and CD45⁺CD11b⁺Ly6C⁺Ly6G⁻ monocytes in brains from WT or *Lcn2*^{-/-} mice from **g**. Dots represent individual mice and error bars represent s.e.m. (Ctrl *n* = 6 mice; WT *n* = 8 mice; *Lcn2*^{-/-} *n* = 7 mice; one-way ANOVA). **k, l**, qPCR analysis of immunosuppressive gene signature in granulocytes isolated from BrM of WT or *Lcn2*^{-/-} mice, following BT-RMS or BT-E0771 injection. Heat maps represent z score of individual genes (melanoma: Ctrl *n* = 5 mice, WT *n* = 6 mice, *Lcn2*^{-/-} *n* = 6 mice; breast: Ctrl *n* = 3 mice, WT *n* = 5 mice, *Lcn2*^{-/-} *n* = 6 mice).

did not show significant differences in the presence of myeloid cells (Extended Data Fig. 5c), indicating that LCN2-driven recruitment of myeloid cells is a feature of BrM. This is further supported by our finding that G-CSF and GM-CSF, two known granulocyte colony-stimulating factors, were systemically highly upregulated in the blood of BrM-bearing mice from melanoma and breast cancer (Extended Data Fig. 1).

Analysis of the myeloid cell milieu in breast cancer indicated an elevation in recruited monocytes and granulocytes in BrM compared to healthy brains, similarly to melanoma brain metastasis; however, the recruitment of monocytes and granulocytes in breast cancer BrM was not LCN2-dependent (Fig. 5h–j).

Notably, analysis of gene expression in recruited granulocytes isolated from melanoma or breast cancer BrM revealed an upregulation in their expression of an immunosuppressive gene signature in both melanoma and breast cancer BrM in WT mice (Fig. 5k, l). While in melanoma there was no difference in the expression of this immunosuppressive gene signature in *Lcn2*^{-/-} mice (Fig. 5k and Extended Data Fig. 5d), in breast cancer BrM LCN2 was necessary for this functional differentiation of recruited granulocytes (Fig. 5l and Extended Data Fig. 5e). Thus, LCN2 was important for the recruitment of myeloid cells in melanoma brain metastasis; however, their immunosuppressive phenotype was LCN2-dependent in breast cancer, but not in melanoma BrM.

Taken together, these findings show that systemic, as well as local LCN2 in the brain, activate pro-inflammatory signaling in astrocytes, resulting in recruitment of immunosuppressive myeloid cells to the brain metastatic microenvironment.

LCN2 signaling from granulocytes facilitate brain metastasis

Our findings indicated that recruited granulocytes are the main source of LCN2 leading to neuroinflammation in BrM. We therefore asked whether signaling from bone-marrow-recruited granulocytes is functionally important for BrM. We performed adoptive bone-marrow transplantation (BMT) from WT or *Lcn2*^{-/-} mice into lethally irradiated WT mice. Following BMT, mice were injected with melanoma cells and analyzed for BrM, systemic levels of LCN2, astrocyte inflammatory activation and myeloid cell composition in the brain metastatic microenvironment (Fig. 6a). To further validate the specific source of LCN2 in bone marrow, we isolated multiple cell populations from WT bone

marrow and analyzed their expression of *Lcn2*. The results confirmed that bone-marrow-derived LCN2 originates mainly from granulocytes (Extended Data Fig. 6a, b). Moreover, analysis of LCN2 blood levels 1 or 2 weeks following BMT (before melanoma cell injection) revealed that basal LCN2 levels were abolished in blood of mice transplanted with *Lcn2*^{-/-} bone marrow, confirming that bone-marrow-derived cells are the main source of LCN2 (Extended Data Fig. 6c). Following BMT, mice were injected intracardially with melanoma cells and followed up for BrM. Of note, MRI and metastatic burden analysis revealed that mice transplanted with *Lcn2*^{-/-} bone marrow had significantly reduced BrM burden, confirming that LCN2 from bone-marrow-recruited cells is instrumental to support BrM (Fig. 6b–e). Notably, analysis of LCN2 blood levels at end-stage revealed elevation in mice transplanted with WT bone marrow compared to its levels at day 14 and also some elevation of LCN2 in mice transplanted with *Lcn2*^{-/-} bone marrow (Fig. 6f and Extended Data Fig. 6d), consistent with our findings that brain endothelial cells also express *Lcn2* in BrM. We next asked whether granulocyte-derived LCN2 is functionally important for inflammatory activation of astrocytes. Analysis of cytokine and chemokine expression in astrocytes that were isolated from BrM revealed that while astrocytes from mice transplanted with WT bone marrow had significant activation of pro-inflammatory signaling, BMT from *Lcn2*^{-/-} abolished this activation (Fig. 6g and Extended Data Fig. 6e). Furthermore, analysis of the combined 'inflammatory score' confirmed that inflammatory signaling was lower in astrocytes isolated from *Lcn2*^{-/-} bone-marrow-transplanted mice and the inflammatory score of astrocytes significantly correlated with neutrophil infiltration (Fig. 6h, i). Moreover, analysis of myeloid cells in BrM of mice transplanted with WT or *Lcn2*^{-/-} bone marrow indicated enhanced recruitment of monocytes and granulocytes to BrM of mice transplanted with WT bone marrow, which was significantly reduced in mice transplanted with *Lcn2*^{-/-} bone marrow (Fig. 6j–m). Thus, LCN2 is important for recruitment of granulocytes and monocytes to BrM and recruited LCN2-expressing granulocytes play a central functional role in melanoma brain metastatic progression.

LCN2 is a prognostic marker in human brain metastasis

Finally, we analyzed LCN2 signaling in human patients with brain metastasis from melanoma, lung and breast cancer, which are among

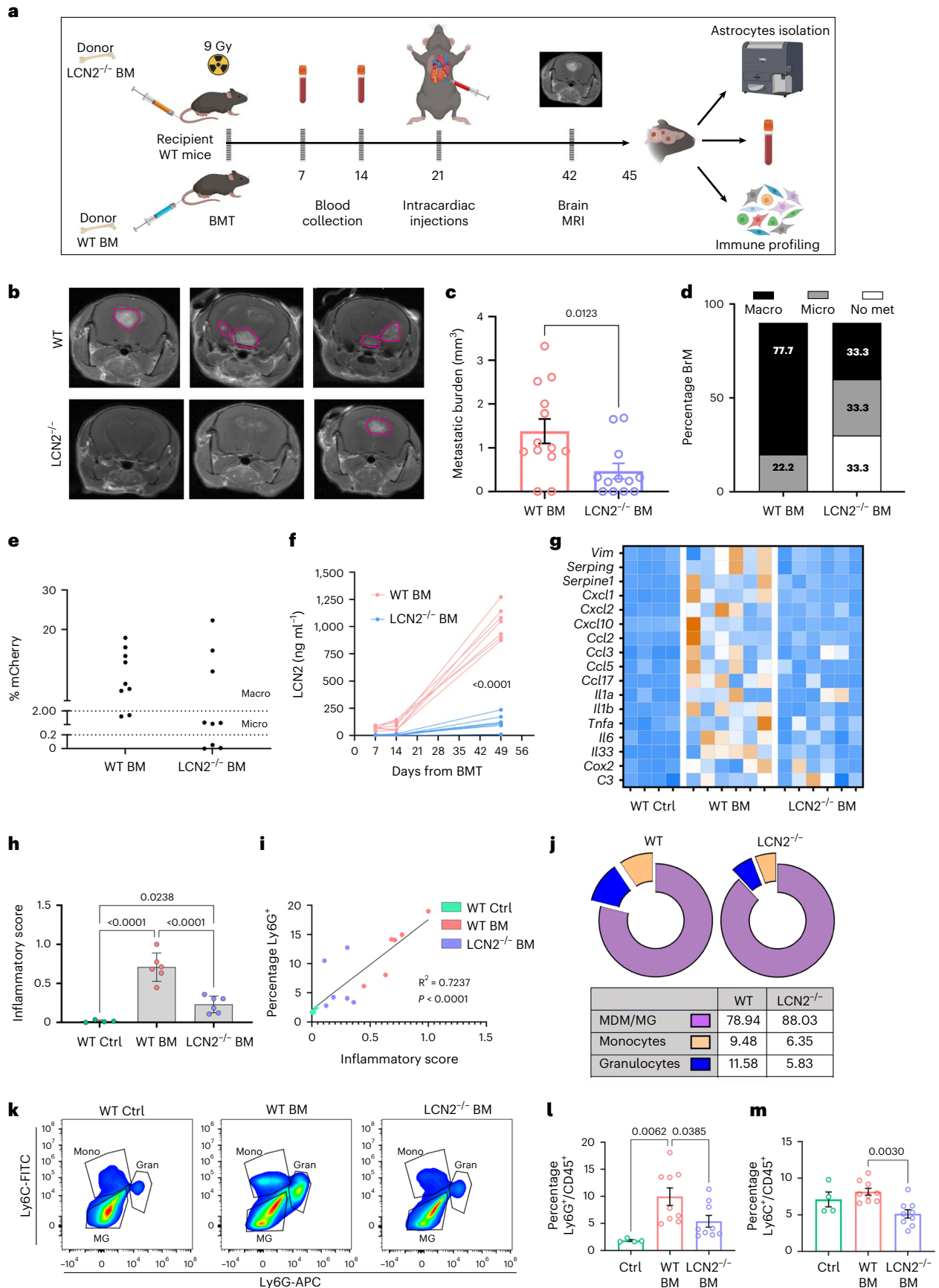
Fig. 6 | LCN2 signaling from bone-marrow-derived cells plays a key functional role in facilitating brain metastasis.

a, Experimental scheme analyzed in **b–i**. Lethally irradiated WT recipient mice received WT or *Lcn2*^{-/-} whole bone marrow (BM), injected intracardially with BT-RMS and analyzed. **b, c**, Representative MRI and quantification of metastatic area, 21 d after injection of BT-RMS cells (WT BM *n* = 13 mice, *Lcn2*^{-/-} BM *n* = 12 mice), error bars represent s.e.m. (Student's *t*-test, two-sided). **d, e**, Brain metastatic (met) incidence quantification. Macrometastases (macro) were defined by positive MRI and flow cytometry detection. The cutoff for micrometastases (micro) was determined by percentage CD45⁺ mCherry⁺ tumor cells in healthy WT mice (WT BM *n* = 9 mice, *Lcn2*^{-/-} BM *n* = 9 mice). **f**, LCN2 plasma levels of mice at different time points following BMT, measured by ELISA (WT BM *n* = 8 mice, *Lcn2*^{-/-} BM *n* = 10 mice; repeated measure ANOVA). **g**, qPCR analysis of inflammatory gene signature in

FACS-sorted astrocytes from WT mice that underwent BMT as described in **a**. Heat maps represent z score of individual genes (Ctrl *n* = 4 mice, WT *n* = 6 mice, *Lcn2*^{-/-} *n* = 6 mice). **h**, qPCR analysis of inflammatory gene signature of mice in **g**, calculated as 'inflammatory score'. Error bars represent s.e.m. (one-way ANOVA). **i**, Two-sided Pearson correlation was calculated between an 'inflammatory score' in sorted astrocytes and percentage of granulocytes in brains of mice from **g** (Ctrl *n* = 4 mice, WT *n* = 6 mice, *Lcn2*^{-/-} *n* = 6 mice). **j, k**, Immune profiling of CD11b⁺ myeloid cells by flow cytometry of mice injected with BT-RMS cells (WT BM *n* = 9 mice, *Lcn2*^{-/-} BM *n* = 7 mice). **l, m**, Flow cytometry analysis of CD45⁺CD11b⁺Ly6C^{inter}Ly6G⁺ granulocytes and CD45⁺CD11b⁺Ly6C⁺Ly6G⁻ monocytes in mice injected with BT-RMS cells. Error bars represent s.e.m. (Ctrl *n* = 4 mice, WT BM *n* = 9 mice, *Lcn2*^{-/-} BM *n* = 9 mice; one-way ANOVA). Graphical illustrations were created with BioRender.com.

the main sources for BrM in patients⁶. Tissue sections from surgically resected BrM were immunostained for expression of LCN2 in astrocytes, endothelial cells, granulocytes and tumor cells. The results indicated

that LCN2 in human BrM from all three cancer types was most abundantly expressed in granulocytes and to a lesser extent in endothelial cells in the metastatic microenvironment. It was not expressed in



astrocytes or in tumor cells, validating our results in mouse models (Fig. 7a and Extended Data Fig. 7a). Analysis of a dataset of gene expression in human BrM and primary brain tumors¹⁰ confirmed that granulocytes are the main source of LCN2 in the human brain microenvironment (Fig. 7b,c). Furthermore, in human brain metastasis, CD45⁺ cells were also a prominent source of LCN2 in the brain, compatible with its expression in endothelial cells (Fig. 7b).

We next assessed systemic levels of LCN2 in patients with BrM from melanoma or lung carcinoma (Extended Data Table 3). Analysis of LCN2 in the blood of melanoma patients with BrM confirmed that it was significantly elevated compared to healthy controls (Fig. 7d). Notably, this cohort of patients included a longitudinal follow-up of blood samples from patients with melanoma BrM. Markedly, temporal analysis of individual samples revealed that a prominent increase in LCN2 blood levels in the last follow-up samples closely preceded patient death (Fig. 7e). Intrigued by these findings we analyzed the correlation between patient survival and LCN2 levels at their last follow-up. We found that lower levels of LCN2 correlated with longer survival (Fig. 7f,g), implicating systemic LCN2 as a potential patient follow-up and prognostic marker.

We further analyzed a cohort of patients with BrM from lung cancer to assess whether LCN2 may also function as a prognostic marker in other cancer types. Analysis of blood samples collected from patients with lung cancer before surgical removal of their BrM confirmed that similarly to what we observed in melanoma metastases, LCN2 levels were higher in the blood of patients compared to healthy controls (Fig. 7h). As in this cohort we did not have multiple follow-up blood samples, we analyzed the correlation of the preoperative blood levels of LCN2 with patient survival. Of note, while long-term follow-up indicated that the correlation of LCN2 levels with 5-year survival was not significant (Extended Data Fig. 6b), analysis of 2-year survival rates revealed that high levels of LCN2 significantly correlated with worse survival (Fig. 7i,j). Clinical decisions on the care of patients with BrM often have to integrate multiple factors to determine prognosis and treatment paradigms³⁵, including their functional performance score. We therefore investigated the Karnofsky performance score (KPS) of these patients, which is clinically used to quantify the ability of patients to perform in daily life activities and assess their general wellbeing³⁶. The score ranges from 100 (fully active) to 0 (death). As expected, a lower KPS score (< 70) correlated with worse survival in the cohort that we analyzed (Extended Data Fig. 6c); however, a subpopulation of patients with low KPS score may still benefit from systemic and/or local treatments rather than palliative care. Thus, stratifying this patient group with additional markers may support clinical decision making to define a subgroup that will still benefit from various treatment strategies.

Notably, stratification of patients with low KPS score (< 70) according to their LCN2 levels revealed that high LCN2 was significantly

correlated with poor survival (Extended Data Fig. 7d). To further assess whether LCN2 is specifically prognostic for BrM, we analyzed cohorts of patients with stage IV melanoma who were stratified according to their BrM status. Of note, Cox survival analysis revealed that LCN2 was predictive of survival in patients with BrM but not in patients with extracranial metastasis (Fig. 7k). Moreover, analysis using the graded prognostic assessment (GPA), which includes the KPS score, was not significantly associated with survival. However, in multivariable analysis including both GPA and LCN2, LCN2 remained prognostic while GPA was not significant in predicting survival (Fig. 7k). Further analysis in a cohort of patients with BrM from lung cancer revealed similar results; LCN2 was predictive of survival, whereas GPA alone was not (Fig. 7l). Thus, blood levels of LCN2 are linked with disease progression and outcome in BrM and may provide a new tool to instruct clinical decision on patient care in fragile patients. Taken together, these findings suggest that systemic levels of LCN2 may be clinically used as an additional prognostic marker in the management of brain metastatic disease.

Discussion

Our study uncovers a mechanism by which the reciprocal interactions between recruited innate immune cells and resident astrocytes facilitate BrM in melanoma and breast cancer. We show that granulocytes induce pro-inflammatory activation of astrocytes, mediated by LCN2. Mechanistically, we demonstrated that systemic LCN2 signaling from the primary tumor instigates neuroinflammation in the brain metastatic niche by activation of astrocytes, leading to recruitment of LCN2-producing granulocytes from the bone marrow to the brain metastatic microenvironment (Fig. 8). These functions of LCN2 are critical for BrM, as genetic ablation of LCN2 in mice or BMT from *Lcn2*^{-/-} resulted in significant attenuation of BrM and improved survival. Moreover, we show that LCN2 is a potential diagnostic and prognostic factor in human patients, linked with disease progression and poor survival.

While granulocytes were recently investigated in the microenvironment of primary brain tumors^{8,37,38}, their interactions with astrocytes in BrM are largely unknown. Our findings elucidate a role for recruited granulocytes in astrocyte activation and demonstrate the key functional importance of their signaling for brain metastatic growth.

LCN2 was shown to be upregulated in multiple cancers, including breast, pancreatic and ovarian carcinoma³⁹. Different studies reported LCN2 to have both pro- and anticancer functions, depending on tumor type and stage⁴⁰⁻⁴². The reported tumor-promoting roles of LCN2 are pleiotropic and include pro-angiogenic activity⁴³, enhancement of epithelial-to-mesenchymal transition^{44,45}, mediating cachexia in pancreatic cancer⁴⁶ and sequestration of iron that facilitates tumor cell survival⁴⁵. LCN2 was shown to mediate neuroinflammation and tissue damage response in the CNS⁴⁷; however, although neuroinflammation is a hallmark of brain metastasis⁶, the role of LCN2 in the brain metastatic microenvironment is largely unexplored.

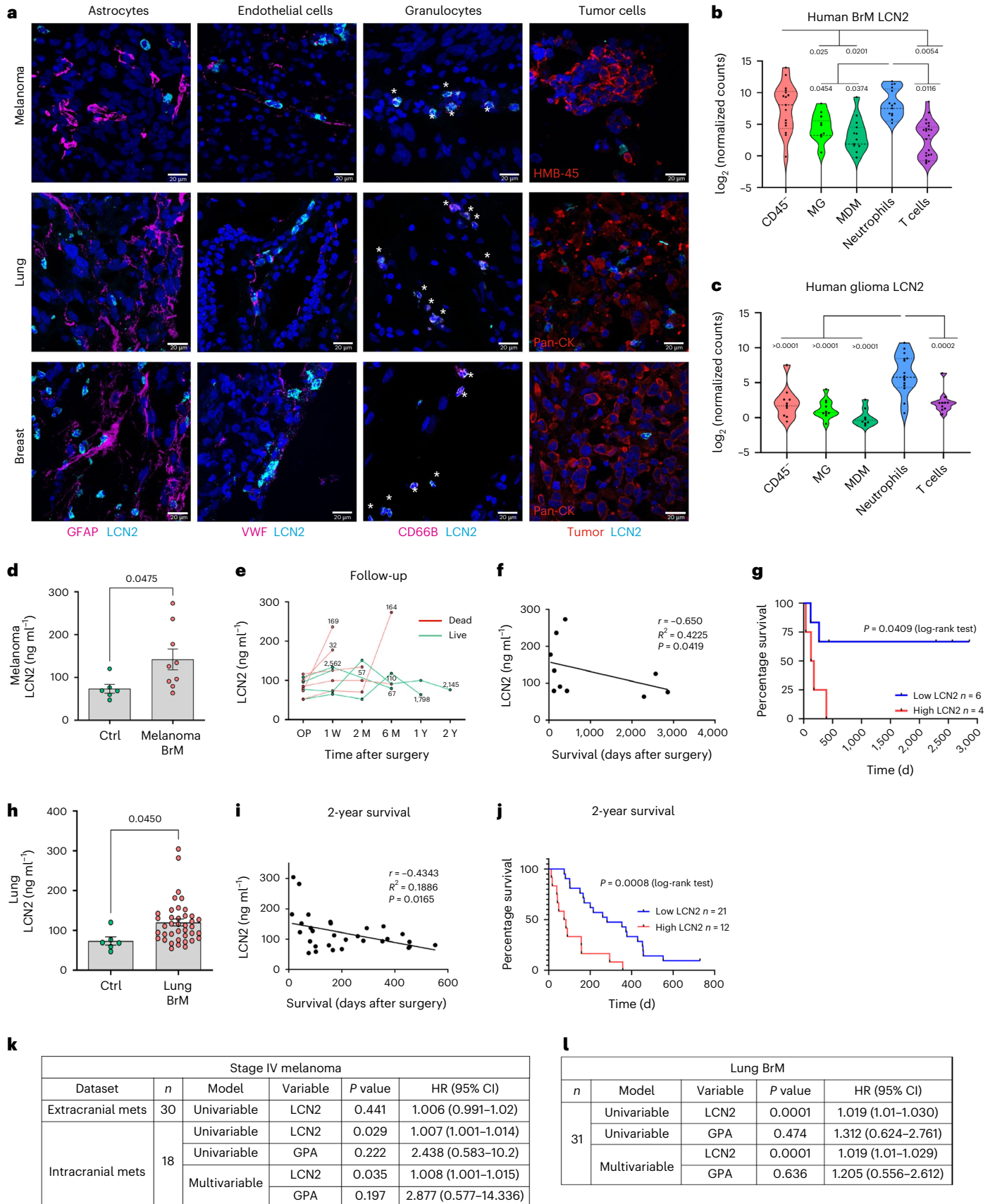
Fig. 7 | Microenvironment-derived LCN2 signaling is operative in human patients and correlates with decreased survival in patients with brain metastases from melanoma, breast and lung primary origin.

a, Immunofluorescence in frozen sections of human brain metastases from melanoma, breast and lung primary origin. Colocalization of LCN2 with specific cell markers: GFAP (astrocytes), HMB45 (melanoma), pan-cytokeratin (breast and lung), VWF (endothelial cells) and CD66b (granulocytes). Representative images are shown from $n = 2$ patients stained per cancer type. **b,c**, LCN2 expression in bulk RNA-seq of different cell populations isolated from samples of human BrM and gliomas (brain TIME dataset), dots represent individual patients (CD45⁺ $n = 17/23$ patients, MG $n = 14/21$ patients, MDM $n = 15/17$ patients, neutrophils $n = 17/16$ patients, T cells $n = 25/22$ patients; one-way ANOVA). **d,h**, LCN2 plasma levels of patients with BrM from melanoma ($n = 9$ patients), lung ($n = 39$ patients) and healthy Ctrl samples ($n = 6$ patients), measured by ELISA. Dots represent individual patients, error bars represent s.e.m. (Student's *t*-test, two-sided). **e**, Longitudinal follow-up of LCN2 plasma levels in patients with melanoma BrM

following surgical resection. Numbers indicate days from last blood sample to death (red) or to last follow-up (green) ($n = 10$ patients). **f**, Two-sided Pearson correlation was calculated between LCN2 plasma levels (measured at the patients last follow-up) and overall survival (OS) of patients in **d,e** ($n = 10$ patients). **g**, Survival curve analysis of patients with low versus high LCN2 levels in patients from **d,e**. The cutoff between high and low levels was defined as the median LCN2 level ($n = 10$ patients; Kaplan–Meier curve, log-rank test). **i**, Two-sided Pearson correlation was calculated between LCN2 plasma levels (measured before BrM resection) and OS of patients in **h** ($n = 30$ patients). **j**, Two-year survival curve analysis of patients with low versus high LCN2 levels in patients from **h**. The cutoff between high and low levels was defined as the median LCN2 level ($n = 33$ patients; Kaplan–Meier curve, log-rank test). **k,l**, Cox proportional hazards model for survival of patients with stage IV melanoma BrM ($n = 18$ patients) or patients with lung cancer BrM ($n = 31$ patients) with LCN2, GPA or a combination of both in a multivariable analysis, using univariable and multivariable analysis. $P = 0.05$.

Our findings in melanoma and breast cancer implicated systemic LCN2 as an inducer and potential prognostic marker of BrM. Specifically, we found that high levels of LCN2 in the CSF are characteristic of BrM and are in correlation with brain metastatic burden. Notably,

LCN2 in human CSF was previously suggested as a prognostic marker for vascular dementia, associated with astrogliosis and inflammatory recruitment of macrophages⁴⁸. Thus, LCN2 in the CSF may be a hallmark of neuroinflammation in multiple pathologies. Of note, LCN2 was shown



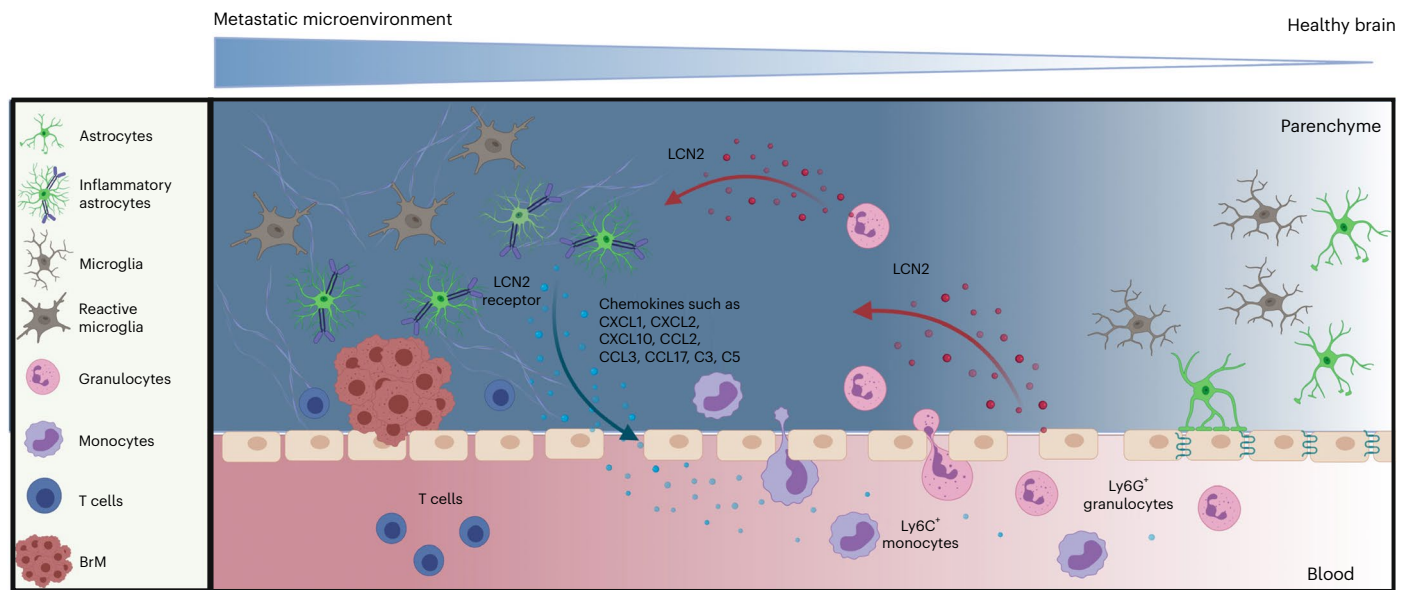


Fig. 8 | Graphical summary. Systemic LCN2 drives an inflammatory activation of astrocytes in the brain metastatic niche, via the LCN2-specific receptor (SLC22A17), leading to recruitment of LCN2-producing granulocytes from the BM

to the brain metastatic microenvironment. Granulocyte-derived LCN2 is central to further enhancing neuroinflammation and brain metastatic progression. Graphical illustrations were created with BioRender.com.

to be upregulated in leptomeningeal metastasis and to provide tumor cells with growth advantage in the nutrient poor environment of the CSF⁴⁹. Consistent with our results, LCN2 in this study was not expressed by macrophages/microglia or by lymphoid cells. We found that in both primary tumors and in BrM, endothelial cells and granulocytes were the main source of LCN2, rather than the cancer cells. Taken together, both studies uncover central roles of LCN2 in facilitating BrM. It is conceivable that LCN2 mediates neuroinflammation in the brain parenchyma, whereas in leptomeningeal disease LCN2 in the CSF also promotes survival of cancer cells via its classical iron-chelating functions.

Investigating the early events that initiate neuroinflammation, we show that stromal cells in the primary tumor give rise to high systemic levels of LCN2, conceivably instigating astrocyte activation. In the brain microenvironment, astrocytes respond to LCN2 signaling in a receptor-specific manner, resulting in upregulation of pro-inflammatory signaling. While we did not further interrogate LCN2-induced signaling in astrocytes, a detailed dissection of the LCN2–SLC22A17 axis via its downstream intracellular signaling would be an interesting future study.

We further show that LCN2 signaling mediates recruitment of immunosuppressive myeloid cells to the brain microenvironment and that in breast cancer BrM, LCN2 was also important for inducing an immunosuppressive phenotype in recruited myeloid cells.

Of note, although granulocyte-derived LCN2 was functionally important for inflammatory activation of astrocytes and for myeloid cell recruitment in both melanoma and breast cancer models, depleting LCN2 resulted in improved survival only in melanoma BrM. A possible explanation for this discrepancy could be the fact that EO771 cells instigated a massive recruitment of monocytes, possibly providing additional pro-inflammatory mechanisms that facilitated metastasis, while melanoma BrM mobilized more granulocytes. Elucidating cancer type-specific pathways in BrM is important for better design of therapeutic strategies.

Within the recruited myeloid cells, granulocytes were the main source of LCN2 signaling, further augmenting astrocyte activation, neuroinflammation and metastatic growth. Indeed, analysis of bone-marrow cells confirmed that granulocytes are the main source of LCN2. Moreover, adoptive BMT from *Lcn2*^{-/-} mice to WT mice was sufficient to reduce metastatic burden in these mice, phenocopying

Lcn2^{-/-} mice, thus implicating granulocyte-derived LCN2 as a central player in orchestrating BrM formation.

While our data from mouse and human BrM indicate that LCN2 mainly originated from granulocytes, other cell types (for example endothelial cells and fibroblasts) in the primary tumor and in the brain metastatic microenvironment also secrete LCN2. Thus, the central role of LCN2 in inflammatory activation of astrocytes and in facilitating BrM, may be a combined effect of LCN2 originating from various cellular sources.

Our findings in mouse models were supported by analysis of blood samples from patients with melanoma; high LCN2 blood levels upon initial diagnosis correlated with worse survival. Of note, longitudinal follow-up of stage IV patients with BrM revealed that elevation in their LCN2 blood levels coincided with patient death. Taken together, our data in mouse models and in human patients suggest that systemic LCN2 has both a functional role in instigating a hospitable inflammatory niche and a prognostic role, correlating with disease progression and outcome.

Patients with brain metastatic relapse have very poor prognosis and their long-term (over 2 years) survival is usually negligible. As such, the clinical decision whether to operate on BrM is complicated³⁵ and dependent on prognosis. Our data implicate LCN2 levels as a strong predictive factor for survival in patients with BrM in multiple cancer types, in addition to routinely used clinical scores. Thus, our findings encourage further prospective clinical testing to establish whether LCN2 can be used as a prognostic or predictive tool in patients with BrM.

In summary, our study elucidates the intricate interactions between systemic inflammatory mediators and the brain metastatic microenvironment and provides insights into the reciprocal communication between glial cells and recruited innate immune cells in the brain metastatic niche, positioning LCN2 as a key factor. The functional and prognostic aspects of LCN2 that we identified in BrM suggest that targeting LCN2 may be an effective therapeutic strategy for inhibition or prevention of brain metastatic relapse.

Methods

Mice

All animal procedures included in the study were granted ethical approval by the Tel Aviv University Institutional Animal Care and Use

Committee. All animals were maintained within the Tel Aviv University specific-pathogen-free facility. *Lcn2*^{-/-} mice (IMSR cat. no. JAX:024630, RRID:IMSR_JAX:024630) were purchased from the Jackson Laboratory and every litter was genotyped. Non-transgenic C57BL/6 mice were purchased from Harlan, Israel. Mice were used for experiments at 6–10 weeks of age, unless otherwise stated. For melanoma experiments, male mice were used and for breast cancer models, female mice were used exclusively.

Human samples

Human patient blood and BrM tissue samples were collected with written informed consent and processed at the Rabin Medical Center, Beilinson Hospital, Israel, in accordance with recognized ethical guidelines, under an approved Institutional Review Board (0311-20-RMC) or at the Göttingen University Hospital, Germany under an approved Institutional Review Board (24-10-05). Melanoma specimens were obtained from patients with stage II, III or IV melanoma participating in a single-center observational clinical trial authorized by the Ethics Committee of the University of Regensburg, Germany (16-101-0125).

Cell lines

RMS cells²⁰ and their derivative BT-RMS and sBT-RMS¹³ were grown in RPMI medium. E0771 were purchased from the ATCC (CRL-3461). Their derivative (BT-E0771) was generated by two cycles of in vivo selection using intracardiac injection, isolation, culture and re-injection of brain metastatic cells. Cells were grown in RPMI medium. C166 endothelial cells were purchased from ATCC (CRL-2581) and grown in supplemented RPMI medium. Cell lines were not authenticated in our laboratory. All cell lines were grown at 37 °C and 5% CO₂ and routinely tested for *Mycoplasma*.

Cytokine array and analysis

Plasma samples from healthy or BrM-bearing mice were diluted 1:5. Proteome Profiler Mouse XL Cytokine Array was performed according to the manufacturer's protocol (ARY028, R&D). Quantification was obtained by ImageJ software. The VarElect platform²⁶ was utilized to analyze proteins that were upregulated at least twofold in both breast cancer and melanoma with the queries neuroinflammation and metastasis.

Primary cells

Dermal fibroblasts were isolated from ears of 8–12-week-old male C57BL/6J mice as previously described⁵⁰. All experiments were performed with low-passage (p2–4) fibroblasts.

Adult astrocytes were isolated from 6–8-week-old C57BL/6 and *Lcn2*^{-/-} mice as previously described¹³. Cells were cultured in 10% FCS RPMI medium supplemented with astrocyte growth supplement (1852-scl, ScienCell). All experiments were performed with low-passage (p2–4) primary cells.

BM-derived myeloid cells were isolated from the femur and tibia of 8-week-old mice. Cells were cultured for 6–8 da with medium supplemented with 20 ng ml⁻¹ recombinant mouse M-CSF (Peprotech) and 0.1 mM non-essential amino acids.

Tissue dissociation

For brains, mice were intracardially perfused with cold PBS, their brains were collected, minced and dissociated using Papaine (LS004182, Worthington Biochemical Corporation), TrypLE (12604013, Thermo Fisher) and DNase (LS002007, Worthington Biochemical Corporation). Red blood cells (RBCs) were lysed using NaCl hypotonic solution. Demyelination was achieved using Percoll (P4937-500ML, Sigma-Aldrich).

For primary tumors, resected melanoma and breast tumors were minced and dissociated using Collagenase type 2 (LS004177, Worthington Biochemical Corporation) and Dispase type 2 (4942078001, Sigma-Aldrich). RBCs were lysed using NaCl hypotonic solution.

ELISA

For mice, an ELISA for mLCN2 was performed using R&D Systems (DY1857) commercial kit, according to the manufacturer's protocol. Plasma samples were diluted 1:2,000, CSF samples were diluted 1:40 and CM samples were not diluted.

For humans, an ELISA for hLCN2 was performed using R&D Systems (DY1757) commercial kit, according to the manufacturer's protocol. Blood samples were diluted 1:200.

Cerebrospinal fluid collection

Approximately 5 µl of CSF samples was obtained from the cisterna magna of mice brains as previously described²⁰. Samples were stored at –80 °C. Only blood-free samples were analyzed.

Flow cytometry

Single-cell suspensions were incubated with specific fluorophore-conjugated antibodies (detailed in the Reporting Summary) and DAPI (MBD0015; Sigma-Aldrich). Samples were analyzed with Cytoflex LX, Beckman Coulter.

Fluorescence-activated cell sorting (FACS) sorting

Single-cell suspensions of mouse brains were stained with specific fluorophore-conjugated antibodies (detailed in the Reporting Summary) and DAPI (MBD0015; Sigma-Aldrich). Cancer cells were labeled with mCherry (melanoma) or tdTomato (breast). Different cell populations were isolated according to the gating strategy presented in the extended data figures. Sorting was performed with BD FACSaria III Cell Sorter, BD Biosciences.

RNA isolation and qRT-PCR

RNA from sorted cells was isolated using the EZ-RNAl Kit (20-410-100, Biological Industries). RNA from in vitro experiments and from total primary tumors was isolated using the PureLink RNA Mini kit (Invitrogen; 12183018A). Complementary DNA synthesis was conducted using qScript cDNA Synthesis kit (Quanta, 95047-100). Quantitative PCR with reverse transcription (qRT-PCR) was conducted using PerfeCTa SYBR Green Fastmix ROX (Quanta, 95073-012). Expression results were normalized to *Gusb*, *Gapdh* or *Ubc* and to controls. RQ (2^{-ΔΔC_t}) was calculated. The primer list is in Supplementary Table 1.

Inflammatory score calculation

The expression levels of multiple pro-inflammatory genes (including *Cxcl1*, *Cxcl2*, *Cxcl10*, *Ccl2*, *Ccl3*, *Ccl17*, *Il1a*, *Il1b*, *Tnfa*, *Il6*, *Cox2*, *C3* and *C5*) were incorporated into a combined inflammatory score. The z score expression average was calculated for each sample and samples were assigned ranking according to a min–max scale.

Immunostaining

Processing of mouse tissue. Brains were collected, washed in PBS, examined by gross inspection for metastatic lesions and incubated for 5 h in 4% PFA (Electron Microscopy Sciences) then transferred to 1% PFA overnight. Brains were incubated in 0.5 M sucrose for 1 h, then in 1 M sucrose overnight. All incubations were performed at 4 °C. Brains were embedded in Optimal Cutting Temperature compound (Tissue-Tek) on dry ice, then stored at –80 °C.

Processing of human tissue. Resected brain metastases were immediately frozen and maintained in liquid nitrogen at the Rabin Medical Center, Beilinson Hospital BioBank. Tissues were collected and processed as described above for mice tissue. Then, 10-µm serial sections were cut using a cryostat (CM1950, Leica) and slides were stored at –80 °C.

Frozen brain tissue sections were incubated at 60 °C for 30 min, washed with PBS-T, then blocked with PBS with 1% BSA and 5% donkey serum for 30 min. Slides were incubated overnight at 4 °C with specific

antibodies (detailed in the Reporting Summary). Slides were washed with PBS-T and incubated for 1 h at room temperature with specific antibodies (detailed in the Reporting Summary). Stained slides were mounted with DAPI Fluoromount-G (0100-20, Southern Biotech), left to dry for 2 h at room temperature and stored at 4 °C. Images were acquired using the confocal ZEISS LSM800 platform, with a $\times 40/1.4$ oil objective or a $\times 20/0.75$ air objective, or by using the Leica Aperio VERSA slide scanner with a $\times 20$ magnification. All images were analyzed using ImageJ software (ImageJ, RRID [SCR_003070](https://scicrx.org/RRID/SCR_003070)).

Orthotopic tumor transplantations

For melanoma, 5×10^5 low-passage BT-RMS cells were inoculated intradermally as previously described²⁰. Tumor volumes were calculated using the formula $X^2 \times Y \times 0.5$ (where X is the smaller diameter and Y is the larger diameter).

For breast, 5×10^5 BT-EO771 cells were inoculated into the mammary glands as previously described⁵¹. Tumors were resected 3 weeks following injection.

Mice were killed when tumors were <15 mm in diameter, according to the Tel Aviv University Institutional Animal Care and Use Committee guidelines.

Intracardiac injections

8-week-old C57BL/6 or *Lcn2*^{-/-} mice were anesthetized with ketamine/xylazine. Males were injected with 1×10^5 BT-RMS and females with 2×10^5 BT-EO771 cells in 50 μ l PBS into the left ventricle of the heart under an ultrasound guidance. Mice were weighed every other day and monitored for neurological symptoms.

Recombinant LCN2

Cloning and expression protocols were based on our previously described techniques for antibody cloning and expression in Expi293 mammalian cells⁵². Briefly, the amino acid sequence of mouse LCN2 was recovered from the National Center of Biotechnology Information (accession code [34328049](https://www.ncbi.nlm.nih.gov/nuccore/34328049)). A DNA cassette corresponding to codons 21–200 of that sequence (excluding the leader sequence), with optimization for expression in HEK293 cells was purchased from IDT. The cassette with a sequence coding for six consecutive histidine residues (His tag) was cloned into pcDNA3.4 with a human immunoglobulin heavy chain leader sequence by Gibson assembly according to the recommendations of the supplier (NEB). The resulting plasmid (named pcDNA3.4-muLCN2₂₁₋₂₀₀-Ct-His) was introduced by transient transfection into Expi293 mammalian cells as described⁵². Medium was collected 6 d after transfection and recombinant LCN2 (rLCN2) was purified by Ni-NTA affinity chromatography on a 5-ml HisTrap FF column (GE). Following purification and buffer exchange into sterile PBS by PD-10 gel filtration (GE), purified rLCN2 was stored in small aliquots at -80 °C.

Migration assay

Overall, 1×10^5 astrocytes per well were seeded at the bottom chamber of 24-Transwell membrane plates, coated with PDL (Santa Cruz, 136156). Astrocytes were treated with 10 μ g ml⁻¹ recombinant LCN2 for 24 h. Then, 5×10^5 BM-derived cells were placed at the upper chamber. Assays were performed with 5- μ m pore Transwell inserts. Migrated cells were stained for CD45, CD11b, Ly6G, Ly6C and DAPI, followed by flow cytometry analysis.

Primary astrocyte siRNA transduction

Primary adult astrocytes were transfected with a mix of four different *Slc22a17* siRNA clones (Dharmacon Accell SMARTpool, E-002000-00-0020) or with non-targeting siRNA (Dharmacon Accell non-targeting Pool, D-001910-10-20) in Accell Delivery Medium (B-005000-100) for 72 h according to the manufacturer's protocol. The efficiency of *Slc22a17* siRNA KD was analyzed by qRT-PCR.

bone-marrow transplantations

The 8-week-old male C57BL/6 WT mice were lethally irradiated using an X-ray machine (160HF; Philips) at a total dose of 9 Gy. At 24 h after irradiation, mice were injected intravenously (i.v.) with 2.0×10^6 unfractionated BM cells collected aseptically from flushed femurs and tibiae of age-matched C57BL/6 WT or *Lcn2*^{-/-} male mice. Following transplantation, mice received antibiotics for 4 weeks in drinking water (enrofloxacin; 0.2 mg ml⁻¹). To ensure radiation lethality, one mouse of each group was irradiated without transplantation. Three weeks after transplantation, mice were anesthetized with ketamine/xylazine and injected intracardially with 1×10^5 BT-RMS cells. Mice were weighed every other day. At 17 d following injections, mice underwent MRI and were killed 4 d later.

MRI

Mice were anesthetized by isoflurane. T1-weighted images with contrast agent (Magnetol, Gd-DTPA, Soreq MRC Israel Radiopharmaceuticals) were taken by 4.7T MRI-MRS 4000 (MR Solutions). Tumor volume was calculated using Radiant Dicom Viewer 2020.1.1.

Human RNA-seq data analysis

The complete raw count matrix of all sorted populations and the full clinical annotation was downloaded as csv files from the publicly available Brain TIME dataset¹⁰. The expression level of specific genes of interest was analyzed across all available different cell populations.

Multivariable analysis and GPA score calculation

Cox proportional hazards models for survival were applied with LCN2 and the GPA where appropriate in univariable and multivariable analysis. We used a P value cutoff of 0.05. We calculated the GPA according to <https://ascopubs.org/doi/pdf/10.1200/JCO.20.01255>, which included KPS, age, number of intracranial metastasis, presence of extracranial metastasis and mutational status of EGFR (lung cohort) or BRAF (melanoma cohorts).

Statistics and reproducibility

All mice included in the analyses were verified for their genotype and inbred mice with more than 2 weeks of age differences were excluded from experiments. Animals used were randomized by cage according to their genotype and the investigators were not blinded to allocation after intervention/treatment was administered and during outcome analysis. No statistical method was used to predetermine sample size, but the sample size was chosen to be adequate to receive significant results as determined by preliminary experiments. Mice that died before experimental end point for unknown reasons were excluded from analysis.

Statistical analyses were performed using GraphPad Prism software (GraphPad Prism, RRID [SCR_002798](https://scicrx.org/RRID/SCR_002798)). All tests were two-tailed. For in vitro experiments, data represent mean and s.d. of at least three separate biological repeats. For in vivo experiments, data represent mean and s.e.m. of at least two separate biological repeats. For data with normal distribution, a Student's t -test/ANOVA (one-way/two-way/repeated measures) was used according to the experimental setup. For data with non-normal distribution, a Kruskal–Wallis test was used. Correlation analysis were performed with Fisher's exact test (2×2 contingency table). A P value of ≤ 0.05 was considered statistically significant.

Reporting summary

Further information on research design is available in the Nature Portfolio Reporting Summary linked to this article.

Data availability

Source data for Figs. 1–7 and Extended Data Figs. 1–7 have been provided as Source Data files.

All other data supporting the findings of this study are available from the corresponding author upon reasonable request. Source data are provided with this paper.

References

- Eichler, A. F. et al. The biology of brain metastases—translation to new therapies. *Nat. Rev. Clin. Oncol.* **8**, 344–356 (2011).
- Cagney, D. N. et al. Incidence and prognosis of patients with brain metastases at diagnosis of systemic malignancy: a population-based study. *Neuro Oncol.* **19**, 1511–1521 (2017).
- Takei, H., Rouah, E. & Ishida, Y. Brain metastasis: clinical characteristics, pathological findings and molecular subtyping for therapeutic implications. *Brain Tumor Pathol.* **33**, 1–12 (2016).
- Doron, H., Pukrop, T. & Erez, N. A blazing landscape: neuroinflammation shapes brain metastasis. *Cancer Res.* **79**, 423–436 (2019).
- Quail, D. F. & Joyce, J. A. Microenvironmental regulation of tumor progression and metastasis. *Nat. Med.* **19**, 1423–1437 (2013).
- Peinado, H. et al. Pre-metastatic niches: organ-specific homes for metastases. *Nat. Rev. Cancer* **17**, 302–317 (2017).
- Wu, A. M. L. et al. Aging and CNS myeloid cell depletion attenuate breast cancer brain metastasis. *Clin. Cancer Res.* <https://doi.org/10.1158/1078-0432.CCR-21-1549> (2021).
- Quail, D. F. & Joyce, J. A. The microenvironmental landscape of brain tumors. *Cancer Cell* **31**, 326–341 (2017).
- Schulz, M., Salamero-Boix, A., Niesel, K., Alekseeva, T. & Sevenich, L. Microenvironmental regulation of tumor progression and therapeutic response in brain metastasis. *Front. Immunol.* **10**, 1713 (2019).
- Klemm, F. et al. Interrogation of the microenvironmental landscape in brain tumors reveals disease-specific alterations of immune cells. *Cell.* **181**, 1643–1660 (2020).
- Valiente, M. et al. The evolving landscape of brain metastasis. *Trends Cancer.* **4**, 176–196 (2018).
- Chen, Q. et al. Carcinoma–astrocyte gap junctions promote brain metastasis by cGAMP transfer. *Nature* **533**, 493–498 (2016).
- Doron, H. et al. Inflammatory activation of astrocytes facilitates melanoma brain tropism via the CXCL10–CXCR3 signaling axis. *Cell Rep.* **28**, 1785–1798 (2019).
- Priego, N. et al. STAT3 labels a subpopulation of reactive astrocytes required for brain metastasis. *Nat. Med.* **24**, 1024–1035 (2018).
- Wasilewski, D., Priego, N., Fustero-Torre, C. & Valiente, M. Reactive astrocytes in brain metastasis. *Front. Oncol.* **7**, 298 (2017).
- Zou, Y. et al. Polyunsaturated fatty acids from astrocytes activate pparγ signaling in cancer cells to promote brain metastasis. *Cancer Discov.* **9**, 1720–1735 (2019).
- Hirata, E. et al. The brain microenvironment induces DNMT1 suppression and indolence of metastatic cancer cells. *iScience.* **23**, 101480 (2020).
- Zhang, L. et al. Microenvironment-induced PTEN loss by exosomal microRNA primes brain metastasis outgrowth. *Nature* **527**, 100–104 (2015).
- Gril, B. et al. Reactive astrocytic S1P3 signaling modulates the blood–tumor barrier in brain metastases. *Nat. Commun.* **9**, 2705 (2018).
- Schwartz, H. et al. Incipient melanoma brain metastases instigate astrogliosis and neuroinflammation. *Cancer Res.* <https://doi.org/10.1158/0008-5472.CAN-16-0485> (2016).
- Flo, T. H. et al. Lipocalin 2 mediates an innate immune response to bacterial infection by sequestering iron. *Nature* **432**, 917–921 (2004).
- Rathore, K. I. et al. Lipocalin 2 plays an immunomodulatory role and has detrimental effects after spinal cord injury. *J. Neurosci.* **31**, 13412–13419 (2011).
- Jang, E. et al. Phenotypic polarization of activated astrocytes: the critical role of lipocalin-2 in the classical inflammatory activation of astrocytes. *J. Immunol.* **191**, 5204–5219 (2013).
- Jang, E. et al. Secreted protein lipocalin-2 promotes microglial M1 polarization. *FASEB J.* **27**, 1176–1190 (2013).
- Suk, K. Lipocalin-2 as a therapeutic target for brain injury: an astrocentric perspective. *Prog. Neurobiol.* **144**, 158–172 (2016).
- Stelzer, G. et al. VarElect: the phenotype-based variation prioritizer of the GeneCards Suite. *BMC Genomics* **17**(Suppl 2), 444 (2016).
- Lee, S. et al. Lipocalin-2 is a chemokine inducer in the central nervous system: role of chemokine ligand 10 (CXCL10) in lipocalin-2-induced cell migration. *J. Biol. Chem.* **286**, 43855–43870 (2011).
- Yan, L., Borregaard, N., Kjeldsen, L. & Moses, M. A. The high molecular weight urinary matrix metalloproteinase (MMP) activity is a complex of gelatinase B/MMP-9 and neutrophil gelatinase-associated lipocalin (NGAL): modulation of MMP-9 activity by NGAL*. *J. Biol. Chem.* **276**, 37258–37265 (2001).
- Fernández, C. A. et al. The matrix metalloproteinase-9/neutrophil gelatinase-associated lipocalin complex plays a role in breast tumor growth and is present in the urine of breast cancer patients. *Clin. Cancer Res.* **11**, 5390–5395 (2005).
- Kubben, F. J. G. M. et al. Clinical evidence for a protective role of lipocalin-2 against MMP-9 autodegradation and the impact for gastric cancer. *Eur. J. Cancer* **43**, 1869–1876 (2007).
- Nuntagawat, C., Leelawat, K. & Tohtong, R. NGAL knockdown by siRNA in human cholangiocarcinoma cells suppressed invasion by reducing NGAL/MMP-9 complex formation. *Clin. Exp. Metastasis* **27**, 295–305 (2010).
- Devireddy, L. R., Gazin, C., Zhu, X. & Green, M. R. A cell-surface receptor for lipocalin 24p3 selectively mediates apoptosis and iron uptake. *Cell* **123**, 1293–1305 (2005).
- Cabedo Martinez, A. I. et al. Biochemical and structural characterization of the interaction between the siderocalin NGAL/LCN2 (neutrophil gelatinase-associated lipocalin/lipocalin 2) and the N-terminal domain of its endocytic receptor SLC22A17. *J. Biol. Chem.* **291**, 2917–2930 (2016).
- Liddel, S. A. & Barres, B. A. Reactive astrocytes: production, function, and therapeutic potential. *Immunity.* **46**, 957–967 (2017).
- Proescholdt, M. A. et al. The management of brain metastases—systematic review of neurosurgical aspects. *Cancers* <https://doi.org/10.3390/cancers13071616> (2021).
- Schag, C. C., Heinrich, R. L. & Ganz, P. A. Karnofsky performance status revisited: reliability, validity, and guidelines. *J. Clin. Oncol.* **2**, 187–193 (1984).
- Blank, A. et al. Microglia/macrophages express alternative proangiogenic factors depending on granulocyte content in human glioblastoma. *J. Pathol.* **253**, 160–173 (2021).
- Khan, S. et al. Role of neutrophils and myeloid-derived suppressor cells in glioma progression and treatment resistance. *Int. J. Mol. Sci.* <https://doi.org/10.3390/ijms21061954> (2020).
- Santiago-Sanchez, G. S. et al. Biological functions and therapeutic potential of lipocalin 2 in cancer. *Int. J. Mol. Sci.* <https://doi.org/10.3390/ijms21124365> (2020).
- Tong, Z. et al. Neutrophil gelatinase-associated lipocalin: a novel suppressor of invasion and angiogenesis in pancreatic cancer. *Cancer Res.* **68**, 6100–6108 (2008).
- Yang, J. et al. Lipocalin 2 promotes breast cancer progression. *Proc. Natl Acad. Sci. USA.* **106**, 3913–3918 (2009).
- Bauvois, B. & Susin, S. A. Revisiting neutrophil gelatinase-associated lipocalin (NGAL) in cancer: saint or sinner? *Cancers* <https://doi.org/10.3390/cancers10090336> (2018).
- Yang, J., McNeish, B., Butterfield, C. & Moses, M. A. Lipocalin 2 is a novel regulator of angiogenesis in human breast cancer. *FASEB J.* **27**, 45–50 (2013).

44. Tyagi, A. et al. Nicotine promotes breast cancer metastasis by stimulating N2 neutrophils and generating pre-metastatic niche in lung. *Nat. Commun.* **12**, 474 (2021).
45. Rodvold, J. J., Mahadevan, N. R. & Zanetti, M. Lipocalin 2 in cancer: when good immunity goes bad. *Cancer Lett.* **316**, 132–138 (2012).
46. Olson, B. et al. Lipocalin 2 mediates appetite suppression during pancreatic cancer cachexia. *Nat. Commun.* **12**, 2057 (2021).
47. Jha, M. K. et al. Diverse functional roles of lipocalin-2 in the central nervous system. *Neurosci. Biobehav. Rev.* **49**, 135–156 (2015).
48. Llorens, F. et al. Cerebrospinal fluid lipocalin 2 as a novel biomarker for the differential diagnosis of vascular dementia. *Nat. Commun.* **11**, 619 (2020).
49. Chi, Y. et al. Cancer cells deploy lipocalin-2 to collect limiting iron in leptomeningeal metastasis. *Science* **369**, 276–282 (2020).
50. Erez, N., Truitt, M., Olson, P., Arron, S. T. & Hanahan, D. Cancer-associated fibroblasts are activated in incipient neoplasia to orchestrate tumor-promoting inflammation in an NF- κ B-dependent manner. *Cancer Cell* **17**, 135–147 (2010).
51. Shani, O. et al. Fibroblast-derived IL33 facilitates breast cancer metastasis by modifying the immune microenvironment and driving type 2 immunity. *Cancer Res.* **80**, 5317–5329 (2020).
52. Birnboim-Perach, R., Grinberg, Y., Vaks, L., Nahary, L. & Benhar, I. Production of stabilized antibody fragments in the *E. coli* bacterial cytoplasm and in transiently transfected mammalian cells. *Methods Mol. Biol.* **1904**, 455–480 (2019).

Acknowledgements

The authors thank Y. Zilberstein from the Faculty Cellular and Molecular Imaging Center for her help with intracardiac injections and mouse imaging. We thank the Rabin Medical Center Biobank and A. Levy-Barda for their support of this research. We also thank E. Vollmer, E. Ostermeier and K. Kronenberg from Regensburg University Hospital and L. Siam, M. Schaffrinski and D. Egert from Göttingen University Hospital, Germany, for their contribution in collecting and processing human samples. The study was supported by grants to N.E. from the Melanoma Research Alliance (award ID 826222), a Breakthrough Award from the US Department of Defense (BCRP award ID W81XWH2110394), Israel Science Foundation Personalized Medicine Program (IPMP no. 3495/19) and a research grant from the Tel Aviv University Cancer Biology Research Center. N.E. and T.P. were supported by a grant from the German Research Foundation (PU 355/4-1). T.P. was supported by SFB/TRR 305/1 (B03).

Author contributions

O.A., Y.Z., H.D. and N.E. conceived of and designed this study. O.A., Y.Z., N.C., T.P. and N.E. developed the methods. O.A., Y.Z., R.B., L.M. and N.C. performed the experiments. G.G., Y.S., T.S., D.M. and L.M. performed formal analysis. A.A.K., S.H., V.Y., S.H., J.A.H., A.B., S.Y.K., L.N, I.B. and T.P. provided resources. O.A., Y.Z., N.C. and N.E. wrote the original draft. O.A., Y.Z., N.C. and N.E. revised and edited the manuscript. N.C. and N.E. administered this project. N.E. supervised the study. All authors discussed the results and provided feedback on the manuscript.

Competing interests

The authors declare no competing interests.

Additional information

Extended data is available for this paper at <https://doi.org/10.1038/s43018-023-00519-w>.

Supplementary information The online version contains supplementary material available at <https://doi.org/10.1038/s43018-023-00519-w>.

Correspondence and requests for materials should be addressed to Neta Erez.

Peer review information *Nature Cancer* thanks Frank Winkler and the other, anonymous, reviewer(s) for their contribution to the peer review of this work.

Reprints and permissions information is available at www.nature.com/reprints.

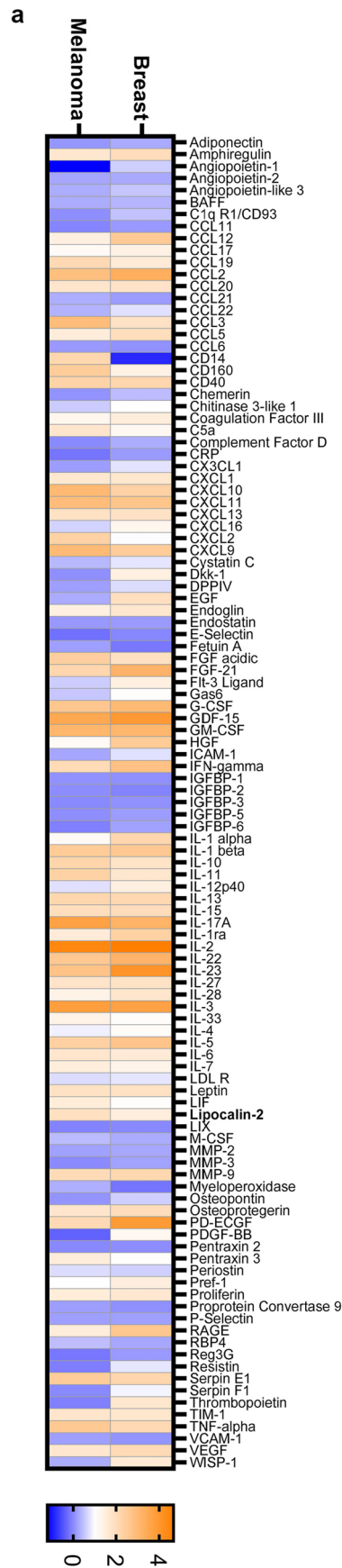
Publisher's note Springer Nature remains neutral with regard to jurisdictional claims in published maps and institutional affiliations.

Springer Nature or its licensor (e.g. a society or other partner) holds exclusive rights to this article under a publishing agreement with the author(s) or other rightsholder(s); author self-archiving of the accepted manuscript version of this article is solely governed by the terms of such publishing agreement and applicable law.

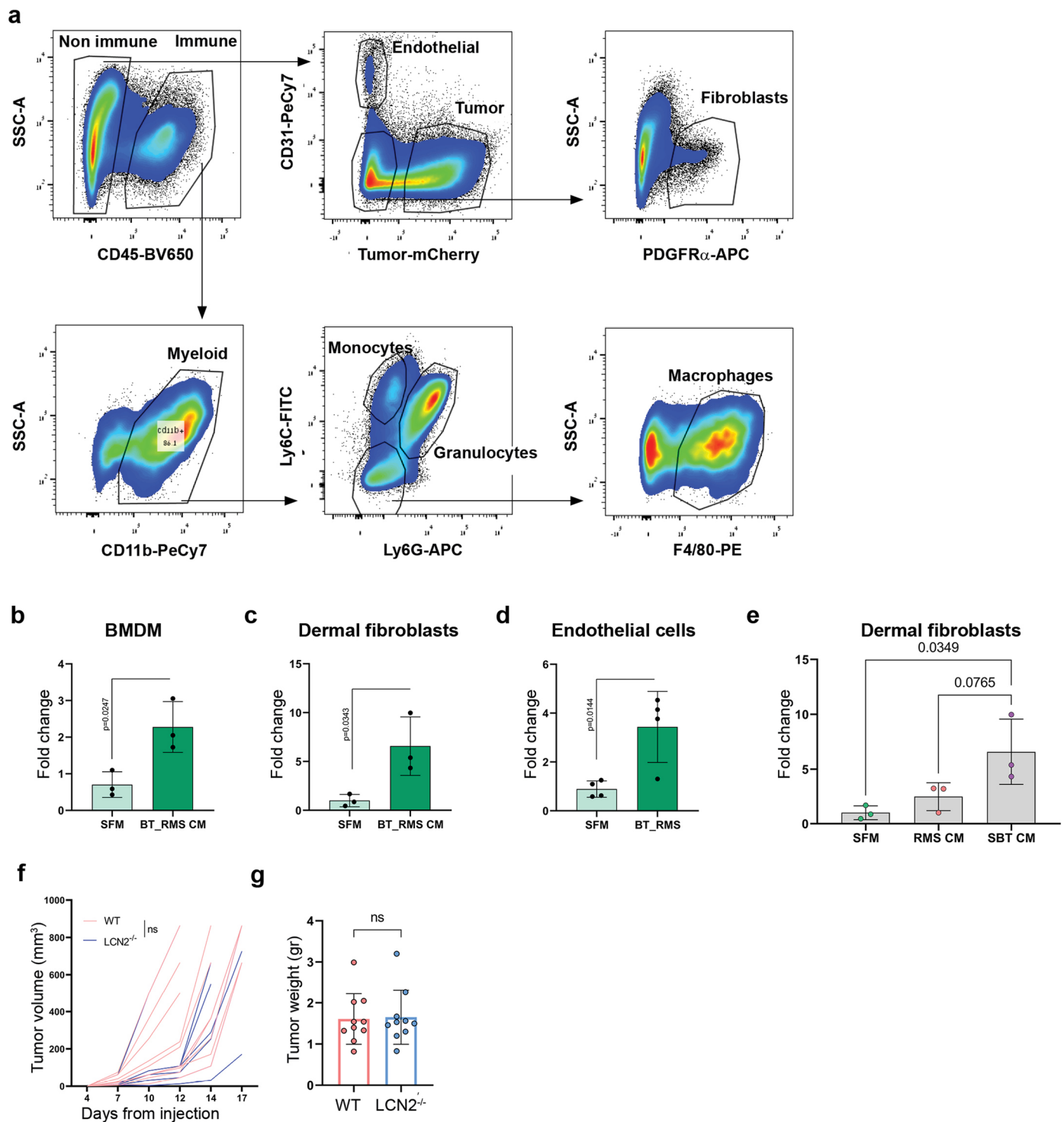
© The Author(s), under exclusive licence to Springer Nature America, Inc. 2023

¹Department of Pathology, Sackler Faculty of Medicine, Tel Aviv University, Tel Aviv, Israel. ²Department of Internal Medicine III, Hematology and Medical Oncology, University Hospital Regensburg, Regensburg, Germany. ³Department of Surgery, University Hospital Regensburg, Regensburg, Germany. ⁴Department of Neurosurgery, Rabin Medical Center and Sackler Faculty of Medicine Tel Aviv University, Tel Aviv, Israel. ⁵Department of Pathology, Rabin Medical Center and Sackler Faculty of Medicine, Tel Aviv University, Tel Aviv, Israel. ⁶Blood Services & Apheresis Institute, Rabin Medical Center and Tel Aviv University, Tel Aviv, Israel. ⁷Department of Dermatology, University Hospital Regensburg, Regensburg, Germany. ⁸Department of Hematology/Medical Oncology, University Medical Center Göttingen, Göttingen, Germany. ⁹Medical Clinic A, Haematology, Haemostasiology, Oncology and Pulmonology, University Hospital Münster, Münster, Germany. ¹⁰West German Cancer Center, University Hospital Münster, Münster, Germany. ¹¹The Shmunis School of Biomedicine and Cancer Research, the George S. Wise Faculty of Life Sciences, Tel Aviv University, Tel Aviv, Israel. ¹²Neuro-Oncology Unit, Davidoff Cancer Center at Rabin Medical Center and Sackler Faculty of Medicine, Tel Aviv University, Tel Aviv, Israel. ¹³Division of Personalized Tumor Therapy, Fraunhofer Institute for Toxicology and Experimental Medicine, Regensburg, Germany. ¹⁴These authors contributed equally: Omer Adler, Yael Zait.

✉ e-mail: netaerez@tauex.tau.ac.il

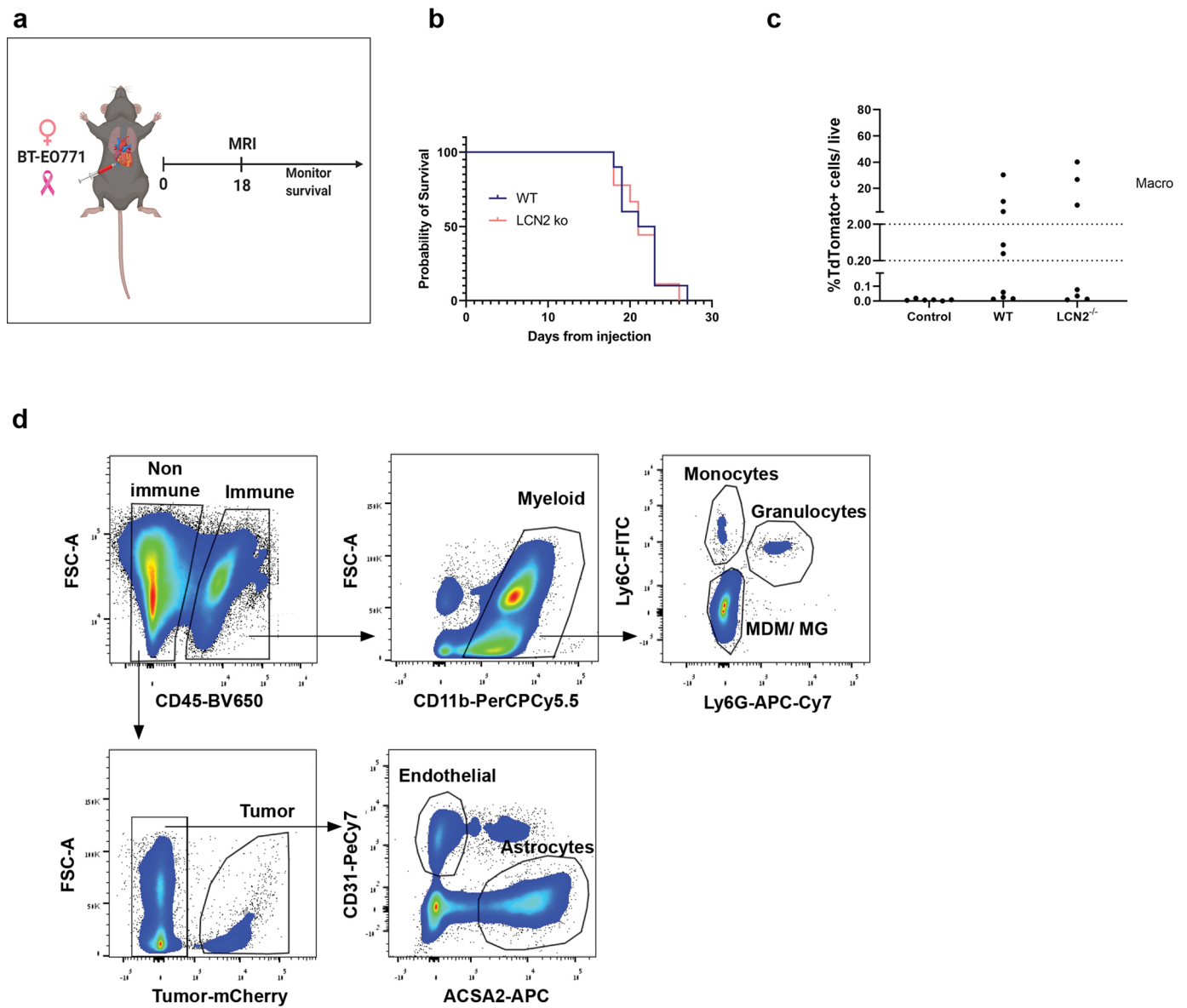


Extended Data Fig. 1 | Proteomic analysis of secreted proteins in blood of mice with melanoma or breast cancer brain metastasis. Heatmap showing fold change values of secreted proteins measured by Proteome profiler Mouse XL Cytokine Array. Mean grey value was quantified by ImageJ. Heatmap represents Log₂ (BrM/Normal) values.



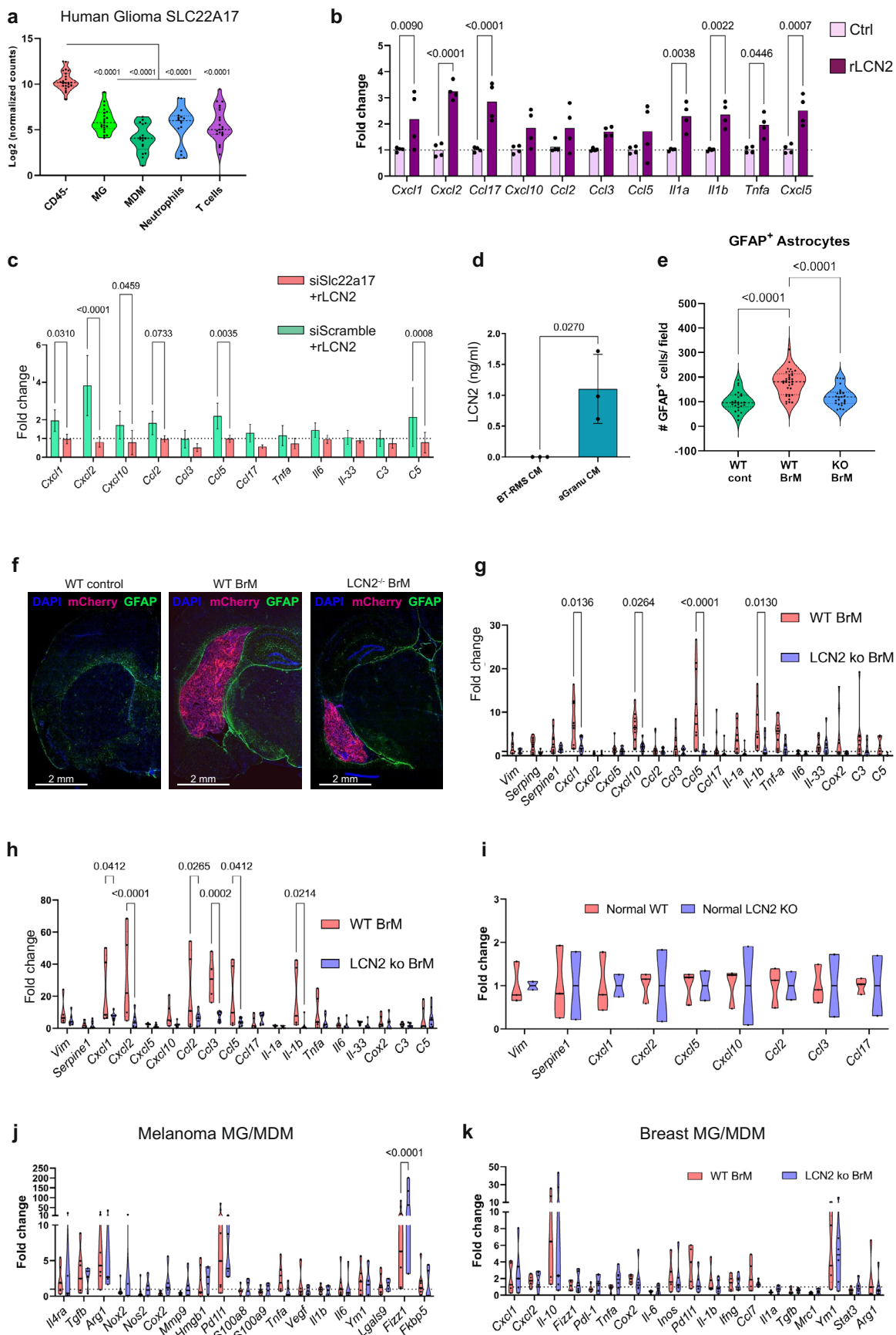
Extended Data Fig. 2 | *LCN2* expression is induced by tumor cell-secreted factors, and is not necessary for primary tumor growth. **a.** Gating strategy for FACS isolation of different cell populations from primary tumors 2.5 weeks following BT-RMS or BT-EO771 orthotopic injection. **b–d.** qPCR analysis of *Lcn2* from BMDM, dermal fibroblasts and C166 endothelial cells treated *in vitro* with BT-RMS CM (BT_RMS CM) versus serum free medium (SFM). 3 biological repeats, error bars represent mean \pm SD (Student's *t*-test, two-sided). **e.** qPCR analysis of *Lcn2* in primary dermal fibroblasts treated with secreted factors from RMS and

SBT-RMS, error bars represent mean \pm SD (SFM $n = 3$, RMS CM $n = 3$, SBT CM $n = 3$ biological replicates) (one-way ANOVA). **f.** Primary tumor growth curve of WT and *Lcn2*^{-/-} mice orthotopically injected with BT-RMS melanoma cells, measured manually by caliper, (WT $n = 10$, *Lcn2*^{-/-} $n = 8$ mice) (Repeated measure ANOVA). **g.** Primary tumor weight at time of resection of WT and *Lcn2*^{-/-} mice orthotopically injected with BT-EO771 cells, (WT $n = 10$, *Lcn2*^{-/-} $n = 10$ mice), dots represent individual mice, error bars represent s.e.m. (Student's *t*-test, two-sided).



Extended Data Fig. 3 | Brain metastatic burden and survival in mice injected with breast cancer cells. **a.** Experimental scheme analyzed in (b,c). **b.** Survival curve analysis of WT and *Lcn2*^{-/-} mice injected intracardially with BT-E0771 cells, (WT *n* = 10, *Lcn2*^{-/-} *n* = 9 mice) (Kaplan–Meier curve, log-rank test). **c.** Quantification of brain metastatic burden for mice in (a), quantified as

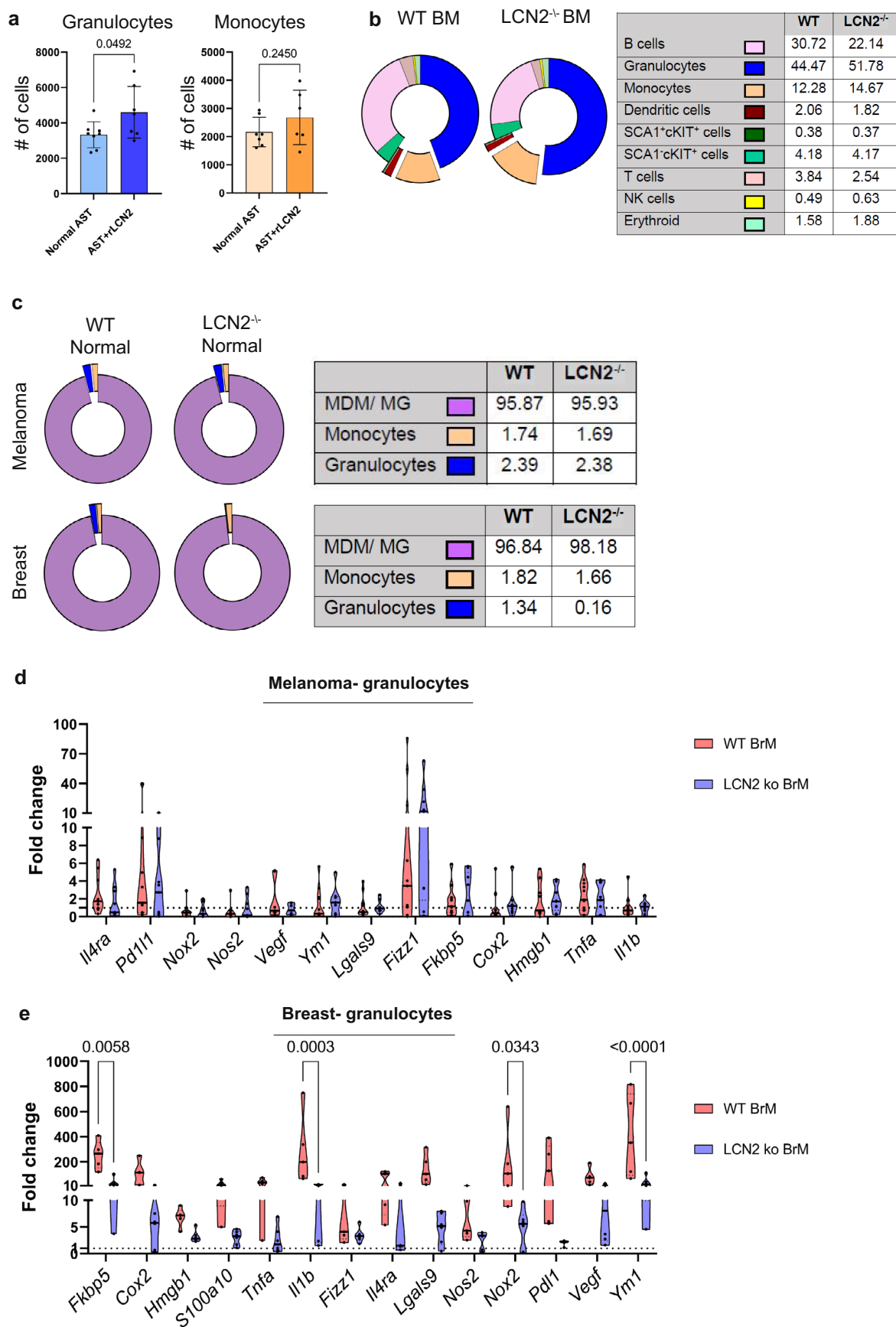
% CD45- mCherry+ tumor cells/live cells, (ctrl *n* = 9, WT *n* = 9, *Lcn2*^{-/-} *n* = 7 mice) (one-way ANOVA). **d.** Gating strategy for isolation by FACS of different cells populations from WT and *Lcn2*^{-/-} BrM mice injected intracardially with BT-RMS or BT-E0771 cells 18 days after injection.



Extended Data Fig. 4 | See next page for caption.

Extended Data Fig. 4 | Astrocytes activate pro-inflammatory signaling in an LCN2-dependent manner, and SLC22A17 is required for astrocyte response to LCN2. **a.** Expression of *SLC22A17* in bulk RNA-seq of different cell populations isolated from samples of human gliomas (CD45- $n = 23$, MG $n = 21$, MDM $n = 17$, Neutrophils $n = 16$, T cells $n = 22$ patients) (one-way ANOVA), (Brain TIME dataset). **b.** LCN2 is sufficient to induce pro-inflammatory signaling in primary astrocytes. qPCR analysis of inflammatory gene signature in primary astrocytes incubated with 10ug/ml rLCN2. Error bars represent SD, dots represent two biological repeats with technical replicates (two-way ANOVA). **c.** qPCR analysis of inflammatory gene signature in primary astrocytes transfected with siRNA targeting *Slc22a17* or with control siRNA (si*Slc22a17* or siScramble). Astrocytes were then treated with 10ug/ml rLCN2 or SFM for 24 h. Error bars represent SD, 4 biological repeats in duplicates. **d.** LCN2 measured in CM of BT-RMS cells or granulocytes activated by BT-RMS CM, error bars represent SD, dots represent 3 biological repeats (two-way ANOVA). **e, f.** Activation of astrocytes was quantified

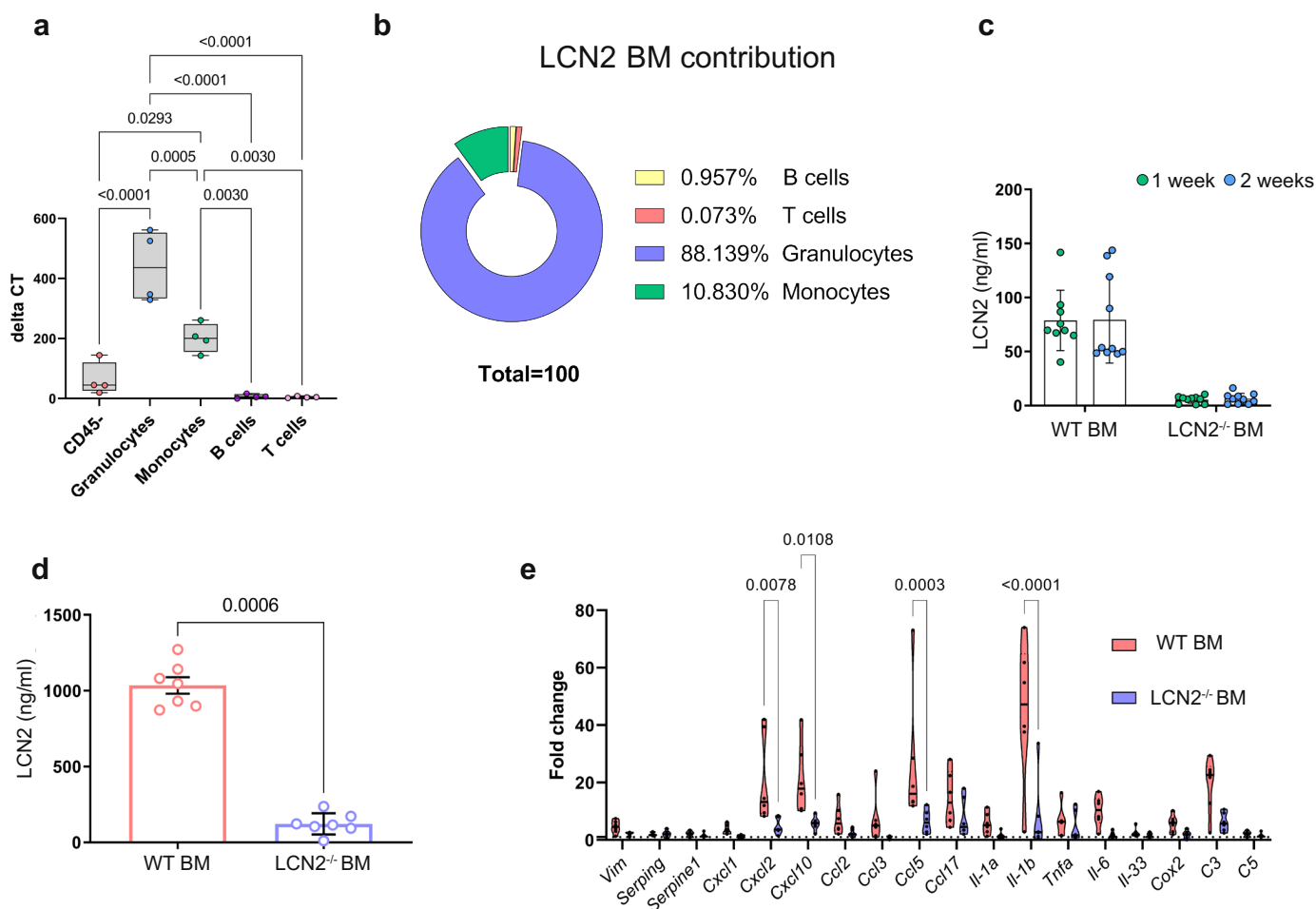
by number of GFAP+ cells/ field. Representative images are shown from $n = 6, 8, 8$ mice per group, error bars represent mean \pm SD. 6 fields X 1 sections per mouse were analyzed (one-way ANOVA). **g, h.** Expression level of inflammatory gene signature measured by qPCR in RNA of FACS sorted astrocytes in vivo from WT or *Lcn2*^{-/-} mice with BrM following BT-RMS or BT-EO771 injection. Dots represent individual mice, line indicates median, plot shows mean to max (melanoma: Ctrl $n = 4$, WT $n = 7, 10$, *Lcn2*^{-/-} $n = 5, 9$ mice), (breast: Ctrl $n = 6$, WT $n = 5$, *Lcn2*^{-/-} $n = 5, 7$ mice) (two-way ANOVA). **i.** Expression level of inflammatory gene signature measured by qPCR of FACS sorted astrocytes in vivo from WT or *Lcn2*^{-/-} normal mice, (WT $n = 3$, *Lcn2*^{-/-} $n = 2$ mice). **j, k.** Expression level of immunosuppressive gene signature measured by qPCR of sorted MG/MDM in vivo from WT or *Lcn2*^{-/-} mice, 3 weeks following BT-RMS or BT-EO771 intracardiac injection, line indicates median, plot shows mean to max (Melanoma WT $n = 7$, *Lcn2*^{-/-} $n = 5$, Breast WT $n = 5$, *Lcn2*^{-/-} $n = 6$ mice) (two-way ANOVA).



Extended Data Fig. 5 | See next page for caption.

Extended Data Fig. 5 | LCN2 induces recruitment of immune suppressive granulocytes to brain in the context of BrM. **a.** Quantification of migrated Ly6G⁺ granulocytes or Ly6C⁺ Ly6G⁻ monocytes toward normal astrocytes or astrocytes treated 24 h with 10ug/ml rLCN2. Dots represent individual wells, 4 biological repeats in duplicates, error bars represent mean \pm SD (Student's *t*-test, two-sided). **b.** Immune profiling of bone marrow cell populations by flow cytometry of 8-week-old C57BL/6 WT or *Lcn2*^{-/-} mice,

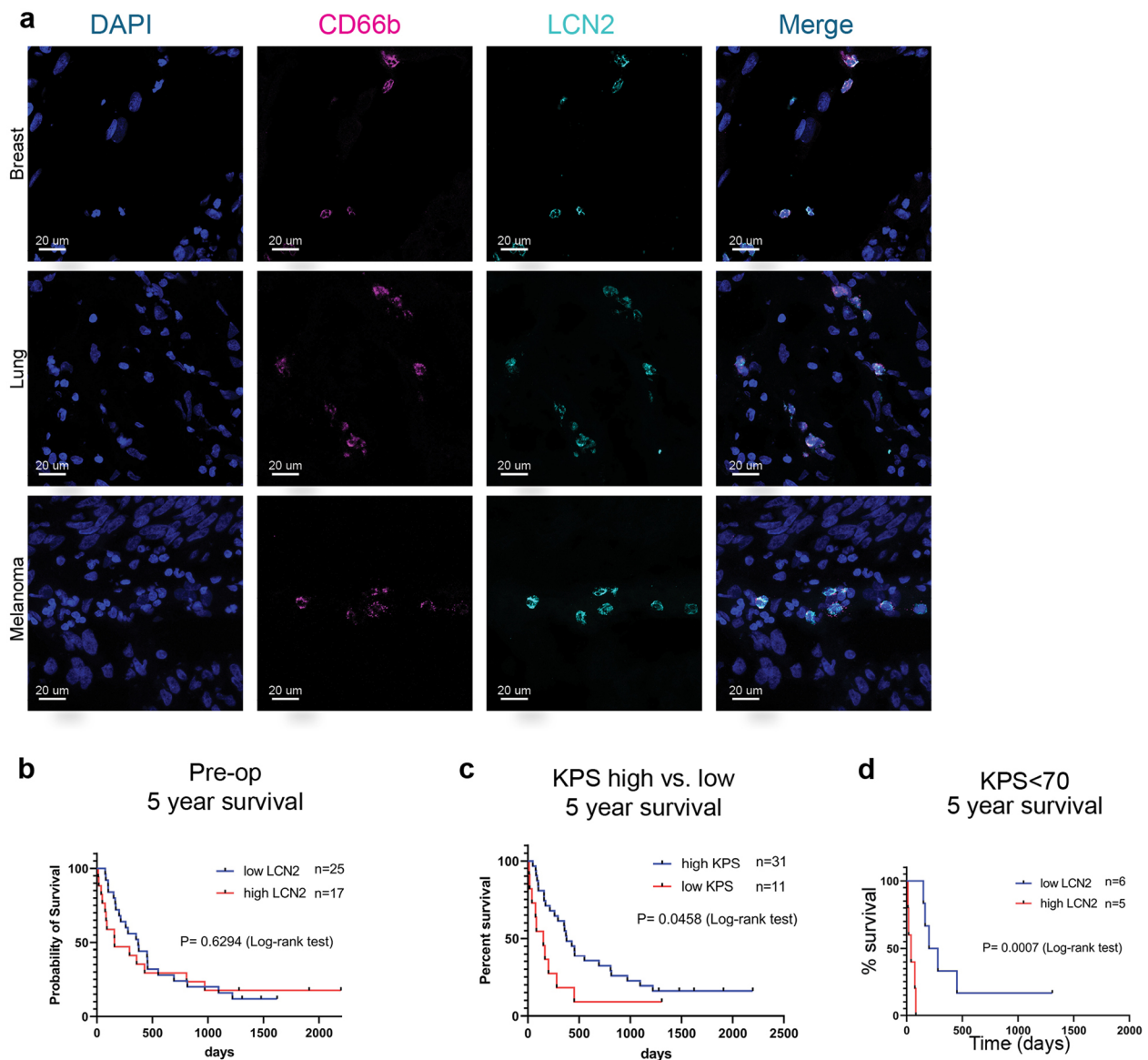
(WT *n* = 5, *Lcn2*^{-/-} *n* = 5 mice). **c.** Immune profiling of CD11b⁺ myeloid cells by flow cytometry of normal WT or *Lcn2*^{-/-} mice (male WT *n* = 5, *Lcn2*^{-/-} *n* = 3, female WT *n* = 6, *Lcn2*^{-/-} *n* = 3 mice). **d,e.** Expression level of immunosuppressive gene signature measured by qPCR of FACS sorted granulocytes *in vivo* from WT or *Lcn2*^{-/-} mice, 3 weeks following BT-RMS intracardiac injection, line indicates median, plot shows mean to max (Melanoma WT *n* = 11, *Lcn2*^{-/-} *n* = 9, Breast WT *n* = 5, *Lcn2*^{-/-} *n* = 6 mice) (two-way ANOVA).



Extended Data Fig. 6 | Bone marrow-derived granulocyte induce increasing systemic LCN2 levels in plasma and inflammatory activation of astrocytes.

a. qPCR analysis of *Lcn2* expression in different cell populations sorted from bone marrow of normal C57BL/6 males: CD45⁻, CD45⁺CD11b⁺Ly6C^{int}Ly6G⁺ granulocytes, CD45⁺CD11b⁺Ly6C⁺Ly6G⁻ monocytes, CD45⁺CD11b⁻CD3⁺B220⁻ T cells, CD45⁺CD11b⁻CD3⁻B220⁺ B cells. Dots represent individual mice ($n = 4$ mice per group), line indicates median, whisker shows mean to max (one-way ANOVA). **b.** 'LCN2 BM contribution' calculated by expression of LCN2 in different cell populations from a, multiplied by their abundance in BM from Extended Data

Fig. 5b. Results are presented as percent of total. **c.** LCN2 ELISA in blood, one and two weeks following BMT. Dots represent individual mice, error bars represent s.e.m., (WT $n = 9$, Lcn2^{-/-} $n = 9$ mice) (one-way ANOVA). **d.** LCN2 levels in blood of mice at endpoint measured by ELISA, (WT $n = 7$, Lcn2^{-/-} $n = 7$ mice), dots represent individual mice, error bars represent s.e.m. (Student's *t*-test, two-sided). **e.** Expression level of inflammatory gene signature measured by qPCR in RNA of FACS sorted astrocytes in vivo from WT mice that underwent BMT as described in (Fig. 4a). Dots represent individual mice, line indicates median, plot shows mean to max (Ctrl $n = 4$, WT $n = 6$, Lcn2^{-/-} $n = 6$ mice) (two-way ANOVA).



Extended Data Fig. 7 | LCN2 is highly expressed in granulocytes in human BrM and can help direct patient's care in combination with clinically used prognostic factors. a. Immunofluorescence staining in frozen sections of resected human brain metastases from melanoma, breast and lung primary origin. Co-localization of LCN2 with CD66b (granulocytes). Representative images of separate staining are shown from $n = 2$ patients samples stained per

cancer type. **b.** Five-year survival curve analysis of patients with low versus high LCN2 levels in patients with lung cancer BrM. The cutoff between high and low levels was defined as the median LCN2 level (Kaplan–Meier curve, log-rank test). **c.** Five-year survival curve analysis of patients with KPS score over or under 70, in patients with lung cancer BrM. **d.** 5-year survival curve analysis of patients with KPS score < 70, stratified to low versus high LCN2 levels in patients from Fig. 7h.

Extended Data Table. 1 | Data of patients with brain metastasis from melanoma, breast and lung cancer

	Beilinson cohort		
	Melanoma (n=3)	Lung (n=6)	Breast (n=5)
Sex			
Male	2(66.6%)	4(66.6%)	0
Female	1(33.3%)	2(33.3%)	5(100%)
Age			
<70	2(66.6%)	2(33.3%)	0
≥70	1(33.3%)	4(66.6%)	5(100%)
Median	76	70.5	61
Extracranial metastases			
Present	3(100%)	5(83.33%)	4(80%)
Absent	0	1(16.66%)	1(20%)
BrM status			
Newly diagnosed	3(100%)	6(100%)	3(60%)
Progressive disease	0	0	2(40%)
Number of BrM			
Mean	2.67	2.67	1.6
Histology			
Small cell		0	
Squamous		0	
Adenocarcinoma		3	
Others		6	

Patient and disease characteristics for a cohort of patients with brain metastases from melanoma, breast and lung cancer origin.

Extended Data Table. 2 | Data of patients with untreated stage IV melanoma

	James cohort
	Melanoma
	(n=50)
Sex	
Male	36(72%)
Female	14(28%)
Age	
<70	35(70%)
≥70	15(30%)
Median	63
Extracranial metastases*	
Present	12(24%) *
Absent	38(76%) *
BrM status	
Present	20(40%)
Absent	30(60%)
Survival in months	
<1 year	39(78%)
>1 year	10(20%)
Median	

Patient and disease characteristics for a cohort of patients with stage IV melanoma patients before treatment.

Extended Data Table. 3 | Data of patients with brain metastasis from melanoma and lung cancer

	Metastasis cohort	
	Melanoma (n=10)	Lung (n=42)
Sex		
Male	7(70%)	24(57.1%)
Female	3(30%)	18(42.9%)
Age		
<70	7(70%)	34(81%)
≥70	3(30%)	8(19%)
Median	60 (42-82)	64 (44-85)
KPS status		
<70	2(20%)	10(23.8%)
≥70	6(60%)	32(76.2%)
Extracranial metastases		
Present	7(70%)	11(26.2%)
Absent	3(30%)	29(69%)
BrM status		
Newly diagnosed	1(10%)	26(61.9%)
Progressive disease	9(90%)	16(38.09%)
Number of BrM		
Mean	1 (1-4)	1 (1-25)
Histology		
Small cell		1
Squamous		1
Adenocarcinoma		30
Others		5

Patient and disease characteristics for a cohort of patients with brain metastases from melanoma and lung cancer origin.

Reporting Summary

Nature Portfolio wishes to improve the reproducibility of the work that we publish. This form provides structure for consistency and transparency in reporting. For further information on Nature Portfolio policies, see our [Editorial Policies](#) and the [Editorial Policy Checklist](#).

Statistics

For all statistical analyses, confirm that the following items are present in the figure legend, table legend, main text, or Methods section.

n/a | Confirmed

- The exact sample size (n) for each experimental group/condition, given as a discrete number and unit of measurement
- A statement on whether measurements were taken from distinct samples or whether the same sample was measured repeatedly
- The statistical test(s) used AND whether they are one- or two-sided
Only common tests should be described solely by name; describe more complex techniques in the Methods section.
- A description of all covariates tested
- A description of any assumptions or corrections, such as tests of normality and adjustment for multiple comparisons
- A full description of the statistical parameters including central tendency (e.g. means) or other basic estimates (e.g. regression coefficient) AND variation (e.g. standard deviation) or associated estimates of uncertainty (e.g. confidence intervals)
- For null hypothesis testing, the test statistic (e.g. F , t , r) with confidence intervals, effect sizes, degrees of freedom and P value noted
Give P values as exact values whenever suitable.
- For Bayesian analysis, information on the choice of priors and Markov chain Monte Carlo settings
- For hierarchical and complex designs, identification of the appropriate level for tests and full reporting of outcomes
- Estimates of effect sizes (e.g. Cohen's d , Pearson's r), indicating how they were calculated

Our web collection on [statistics for biologists](#) contains articles on many of the points above.

Software and code

Policy information about [availability of computer code](#)

Data collection

FACS sorting data was collected with FACSDiva software v8.
FACS analysis data was collected with CytExpert software v2.3.
Microscopy data was collected from Leica Aperio VERSA slide scanner or from ZEISS LSM800 platform.

Data analysis

Analysis of flow cytometry data was done using FlowJo software v10.8.1
Image analysis was done using ImageScope software v12.3.3. or Fiji ImageJ software,
GraphPad Prism software v9.4.1 was used for statistical analysis.
MRI images were analyzed using Radiant Dicom Viewer 2020.1.1.

For manuscripts utilizing custom algorithms or software that are central to the research but not yet described in published literature, software must be made available to editors and reviewers. We strongly encourage code deposition in a community repository (e.g. GitHub). See the Nature Portfolio [guidelines for submitting code & software](#) for further information.

Data

Policy information about [availability of data](#)

All manuscripts must include a [data availability statement](#). This statement should provide the following information, where applicable:

- Accession codes, unique identifiers, or web links for publicly available datasets
- A description of any restrictions on data availability
- For clinical datasets or third party data, please ensure that the statement adheres to our [policy](#)

Source data for Fig. 1-7 and Extended Data Fig. 1-7 have been provided as Source Data files.

All other data supporting the findings of this study are available from the corresponding author upon reasonable request. Further information on research design is available in the Nature Research Reporting Summary linked to this article.

Additional analysis was performed on publically available datasets: Brain TIME (<https://joycelab.shinyapps.io/braintime/>)

Human research participants

Policy information about [studies involving human research participants and Sex and Gender in Research](#).

Reporting on sex and gender

Samples used in this study are from:

- Breast cancer samples were obtained from female patients.
- Melanoma and lung cancer samples were obtained from male and female samples.

Specific distribution of human patients sex is detailed in clinical tables 1-3 in the manuscript.

No sex or gender based analysis was performed in this study and the results presented are applicable for both sex.

Population characteristics

Tissues and blood samples used in this study are from breast, lung and melanoma cancer patients, bearing brain metastases. Patients were alive when specimen were isolated. The specimens were obtained by surgical resection of brain metastases. Blood samples were obtained at various time points, specified throughout the manuscript. Specific characteristics information regarding human patients is detailed in clinical tables 1-3 in the manuscript.

Recruitment

Human patient blood and brain metastases tissue samples were collected with written informed consent and processed at the Rabin Medical Center, Beilinson Hospital, Israel, in accordance with recognized ethical guidelines, under an approved Institutional Review Board (0311-20-RMC), or at the Göttingen University Hospital, Germany under an approved Institutional Review Board (24-10-05). Melanoma specimens were obtained from patients with Stage II, III or IV melanoma participating in a single-center observational clinical trial authorized by the Ethics Committee of the University of Regensburg, Germany (16-101-0125).

Ethics oversight

1. Rabin Medical Center, Beilinson Hospital, Israel, in accordance with recognized ethical guidelines, under an approved Institutional Review Board (0311-20-RMC)
2. Göttingen University Hospital, Germany under an approved Institutional Review Board (24-10-05).

Note that full information on the approval of the study protocol must also be provided in the manuscript.

Field-specific reporting

Please select the one below that is the best fit for your research. If you are not sure, read the appropriate sections before making your selection.

- Life sciences Behavioural & social sciences Ecological, evolutionary & environmental sciences

For a reference copy of the document with all sections, see nature.com/documents/nr-reporting-summary-flat.pdf

Life sciences study design

All studies must disclose on these points even when the disclosure is negative.

Sample size

No statistical method was used to pre-determine sample size, but the sample size was chosen to be adequate to receive significant results as determined by preliminary experiments. In all in vivo experiments the smallest sample size was 10 mice per group.

Data exclusions

Inbred mice with more than two weeks age differences were excluded from experiments, to ensure age matching of tested mice. Mice that died before experimental endpoint for unknown reasons were excluded from analysis.

Replication

All experiments were repeated independently at least 2 successful times. Each individual experiment contained 2 or more biological/technical repeats.

Randomization

Animals used for in-vivo experiments were randomized by cage according to their genotype for different experimental arms.

Blinding

The investigators were not blinded to allocation during experiments and outcome analysis since the students responsible for performing the experiments were involved in its design. Rigorous statistical tools used in the analyses prevented any bias.

Reporting for specific materials, systems and methods

We require information from authors about some types of materials, experimental systems and methods used in many studies. Here, indicate whether each material, system or method listed is relevant to your study. If you are not sure if a list item applies to your research, read the appropriate section before selecting a response.

Materials & experimental systems

n/a	Involvement in the study
<input type="checkbox"/>	<input checked="" type="checkbox"/> Antibodies
<input type="checkbox"/>	<input checked="" type="checkbox"/> Eukaryotic cell lines
<input checked="" type="checkbox"/>	<input type="checkbox"/> Palaeontology and archaeology
<input type="checkbox"/>	<input checked="" type="checkbox"/> Animals and other organisms
<input type="checkbox"/>	<input checked="" type="checkbox"/> Clinical data
<input type="checkbox"/>	<input type="checkbox"/> Dual use research of concern

Methods

n/a	Involvement in the study
<input checked="" type="checkbox"/>	<input type="checkbox"/> ChIP-seq
<input type="checkbox"/>	<input checked="" type="checkbox"/> Flow cytometry
<input type="checkbox"/>	<input checked="" type="checkbox"/> MRI-based neuroimaging

Antibodies

Antibodies used

FACS antibodies: anti-CD45-BV650 1:100 (BioLegend, BLG-103151), anti-CD11b-PeCy7 1:100 (BioLegend, BLG- 101215), anti-Ly6G-APC 1:100 (BioLegend, 127614), anti-Ly6C-FITC 1:100 (BioLegend, 128006), anti-SCA1-APC 1:100 (eBioscience, 17-5981-82), anti-C-Kit-PE 1:100 (eBioscience, 12-1171), anti-Ly6G-APC-Cy7 1:100 (BioLegend, 127624), anti-CD11c-PerCp-Cy5.5 1:100 (eBioscience, 45-0114), anti-CD3-PeCy7 1:100 (BioLegend, 100219), anti-B220-PerCp-Cy5.5 1:100 (BioLegend, 103235), anti-NKp46-APC 1:100 (BioLegend, 137607), anti-CD4-APC-Cy7 1:100 (BioLegend, 100413), anti-CD8-PE 1:100 (eBioscience, 12-0083), anti-TER119-FITC 1:100 (BioLegend, 116205), anti-CD45-BV650 1:100 (BioLegend, BLG-103151), anti-CD11b-PerCP-Cy5.5 1:100 (eBioscience, 45-0112), anti-Ly6G-APC-Cy7 1:100 (BioLegend, 127624), anti-Ly6C-FITC 1:100 (BioLegend, 128006), anti-ACSA2-APC 1:100 (Miltenyi Biotec Cat# 130-102-315, RRID:AB_2651190), anti-CD31-PE-Cy7 1:100 (eBioscience, 25-0311).

Immunofluorescence antibodies: rabbit anti-mouse GFAP 1:800 (Z-0334, Dako), rabbit anti-mouse IBA-1 1:200 (NBP2-19019, Novus), rabbit anti-mouse VWF 1:500 (ab6994, Abcam), rat anti-mouse Ly6G 1:500 (127601, Biolegend), goat anti-mouse LCN2 1:100 (AF1857, R&D), rabbit anti-mouse pP65 1:800 (#3033, Cell Signaling), chicken anti-human GFAP 1:1000 (ab9377, Abcam), goat anti-human LCN2 1:100 (AF-1757, R&D), rabbit anti-human pan-cytokeratin 1:500 (ab9377, Abcam), mouse anti-human Melanoma 1:200 (ab732, Abcam), mouse anti-human CD66B 1:500 (G10F5, Novus), donkey anti-rabbit AF647 1:200 (Jackson ImmunoResearch Labs Cat# 711-605-152, RRID:AB_2492288), donkey anti-goat Dylight-488 1:200 (Jackson ImmunoResearch Labs Cat# 705-486-147, RRID:AB_2616594), donkey anti-rat AF647 1:200 (Jackson ImmunoResearch Labs Cat# 712-605-153, RRID:AB_2340694), donkey anti-mouse AF647 1:200 (Jackson ImmunoResearch Labs Cat# 712-605-153, RRID:AB_2340694).

Validation

All primary antibodies used in this study were validated by the manufacture under the ISO 13485:2016 and MDSAP Certification. Validation data / citations can be found on the manufacture website by searching the antibody catalog number provided in materials and methods section of our manuscript.

Eukaryotic cell lines

Policy information about [cell lines and Sex and Gender in Research](#)

Cell line source(s)

C166 endothelial cells were purchased from ATCC (ATCC® CRL-2581™ RMS (Ret-melanoma sorted) cells and their derivative BT-RMS and sBT-RMS were generated from RET melanoma cells which were a kind gift from Dr. Victor Umanski E0771 were purchased from ATCC (ATCC® CRL-3461™) and it's derivative (BT-E0771) were established in our lab by two rounds of in vivo selection. HEK293 cells was purchased from IDT.

Authentication

Cell lines were not authenticated in our laboratory.

Mycoplasma contamination

All cell lines were routinely tested for mycoplasma using the EZ-PCR-Mycoplasma test kit (Biological Industries; 20-700-20) and confirmed to be negative.

Commonly misidentified lines (See [ICLAC](#) register)

No misidentified cell lines were used in this study.

Animals and other research organisms

Policy information about [studies involving animals](#); [ARRIVE guidelines](#) recommended for reporting animal research, and [Sex and Gender in Research](#)

Laboratory animals	All animals were maintained within the Tel Aviv University Specific Pathogen Free (SPF) Facility. LCN2-/- mice (IMSR Cat# JAX:024630, RRID:IMSR_JAX:024630) were purchased from The Jackson Laboratory and were genotyped in every litter. Non-transgenic C57BL/6 mice were purchased from Harlan, Israel. Mice were used for experiments at 6–10 weeks of age, unless otherwise stated. Only mice with verified genotype were included in experiments. Animals were maintained in specific pathogen-free conditions with controlled temperature/humidity (22°C/55%) environment on a 12-h light-dark cycle and with food and water ad libitum
Wild animals	The study did not involve wild animals.
Reporting on sex	For melanoma experiments male mice were used, and for breast cancer models, female mice were used exclusively.
Field-collected samples	The study did not include samples collected from the field.
Ethics oversight	All Animal procedures included in the study were granted ethical approval by the Tel Aviv University Institutional Animal Care and Use Committee.

Note that full information on the approval of the study protocol must also be provided in the manuscript.

Clinical data

Policy information about [clinical studies](#)

All manuscripts should comply with the ICMJE [guidelines for publication of clinical research](#) and a completed [CONSORT checklist](#) must be included with all submissions.

Clinical trial registration	N/A
Study protocol	N/A
Data collection	N/A
Outcomes	N/A

Dual use research of concern

Policy information about [dual use research of concern](#)

Hazards

Could the accidental, deliberate or reckless misuse of agents or technologies generated in the work, or the application of information presented in the manuscript, pose a threat to:

No	Yes	
<input checked="" type="checkbox"/>	<input type="checkbox"/>	Public health
<input checked="" type="checkbox"/>	<input type="checkbox"/>	National security
<input checked="" type="checkbox"/>	<input type="checkbox"/>	Crops and/or livestock
<input checked="" type="checkbox"/>	<input type="checkbox"/>	Ecosystems
<input checked="" type="checkbox"/>	<input type="checkbox"/>	Any other significant area

Experiments of concern

Does the work involve any of these experiments of concern:

No	Yes	
<input checked="" type="checkbox"/>	<input type="checkbox"/>	Demonstrate how to render a vaccine ineffective
<input checked="" type="checkbox"/>	<input type="checkbox"/>	Confer resistance to therapeutically useful antibiotics or antiviral agents
<input checked="" type="checkbox"/>	<input type="checkbox"/>	Enhance the virulence of a pathogen or render a nonpathogen virulent
<input checked="" type="checkbox"/>	<input type="checkbox"/>	Increase transmissibility of a pathogen
<input checked="" type="checkbox"/>	<input type="checkbox"/>	Alter the host range of a pathogen
<input checked="" type="checkbox"/>	<input type="checkbox"/>	Enable evasion of diagnostic/detection modalities
<input checked="" type="checkbox"/>	<input type="checkbox"/>	Enable the weaponization of a biological agent or toxin
<input checked="" type="checkbox"/>	<input type="checkbox"/>	Any other potentially harmful combination of experiments and agents

Flow Cytometry

Plots

Confirm that:

- The axis labels state the marker and fluorochrome used (e.g. CD4-FITC).
- The axis scales are clearly visible. Include numbers along axes only for bottom left plot of group (a 'group' is an analysis of identical markers).
- All plots are contour plots with outliers or pseudocolor plots.
- A numerical value for number of cells or percentage (with statistics) is provided.

Methodology

Sample preparation

rains: mice were intracardially perfused with cold PBS, their brains were harvested, minced, and dissociated using Papaine (LS004182, Worthington Biochemical Corporation), TrypLE (12604013, Thermo Fisher) and DNase (LS002007, Worthington Biochemical Corporation). RBC were lysed using NaCl hypotonic solution. Demyelination was achieved using percoll (P4937-500ML, Sigma-Aldrich).
 Primary tumors: resected melanoma and breast tumors were minced, and dissociated using Collagenase type 2 (LS004177, Worthington Biochemical Corporation) and Dispase type 2 (4942078001, Sigma-Aldrich). RBC were lysed using NaCl hypotonic solution.
 Single-cell suspensions were incubated with the appropriate anti-mouse antibodies according to the experimental scheme.

Instrument

Samples were analyzed with Cytoflex LX, Beckman Coulter.
 Sorting was performed with BD FACSAria™ III Cell Sorter, BD Biosciences.

Software

FlowJo software, BD

Cell population abundance

Purity of sorted was determined using flow cytometry analysis.

Gating strategy

A figure describing gating strategy for selecting cells and singlets is provided in the supplementary information. Boundaries between positive staining and negative staining was determined using and Iso-type control for each antibody used.

- Tick this box to confirm that a figure exemplifying the gating strategy is provided in the Supplementary Information.

Magnetic resonance imaging

Experimental design

Design type

Mice brain metastatic burden was quantified using MRI imaging

Design specifications

Mice were anesthetized by isoflurane. T1 weighted images with contrast agent (Magnetol, Gd-DTPA, Soreq M.R.C Israel Radiopharmaceuticals) were taken.

Behavioral performance measures

Our study did not involve any behavioral features, and therefore we did not performed any analysis in this field.

Acquisition

Imaging type(s)

T1 weighted images with contrast agent (Magnetol, Gd-DTPA, Soreq M.R.C Israel Radiopharmaceuticals) were taken by 4.7T MRI—MRS 4000™ (MR solutions)

Field strength

4.7T MRI—MRS 4000™ (MR solutions)

Sequence & imaging parameters

FSE T1w pulse sequence type, 25x25 field of view, 256R 252P 1S matrix size, 1mm thickness, TR=1150,TE=11,FA=90.

Area of acquisition

Whole brain scan was used

Diffusion MRI

Used

Not used

Preprocessing

Preprocessing software

Tumor volume was calculated using Radiant Dicom Viewer 2020.1.1.

Normalization

Data was not normalized, since we measured the total metastatic area in whole brains of every individual mice and then compared the mean volume of different experimental arms.

Normalization template

Data was not normalized

Noise and artifact removal

Volume censoring

Statistical modeling & inference

Model type and settings

Effect(s) tested

Specify type of analysis: Whole brain ROI-based Both

Statistic type for inference (See [Eklund et al. 2016](#))

Correction

Models & analysis

n/a | Involved in the study

Functional and/or effective connectivity

Graph analysis

Multivariate modeling or predictive analysis